Supplementary Information for Stochastic Turing patterns in a synthetic bacterial population

David Karig et al. 10.1073/pnas.XXXXXXXXXX

1. System design

Turing-type pattern formation is based on short range activation and long range inhibition in a system of interacting "morphogen" species. As shown by Gierer and Meinhardt, one short range, dissipative "activator" morphogen must be autocatalytic, and there are two general possibilities for the longer range morphogen (1). In one type of system, the longer range species inhibits the activator. Alternatively, the longer range species may serve as a substrate necessary for catalysis of the activator, and the long range inhibition effectively occurs through depletion of this substrate. Implementing Turing pattern formation in cells requires two non-interacting intercellular signaling pathways such that one signal serves as the "activator," while the other serves as either the "inhibitor" or "substrate." We chose to use elements from the Las and Rhl quorum sensing systems of *Pseudomonas aeruginosa*, such that $A_{3OC12HSL}$ is effectively the "activator" and I_{C4HSL} is the "inhibitor" (Fig. S1a). Evidence suggested that certain promoters in *P. aeruginosa* respond specifically to either I_{C4HSL}/RhlR or $A_{3OC12HSL}$/LasR (2–4). These systems were also appealing due to the different diffusion properties of the $A_{3OC12HSL}$ and I_{C4HSL} signal molecules (5). We explore these signal specificity and diffusion aspects in detail in later sections.

Designing complex multicellular systems such as a Turing pattern formation system requires the use of computational modeling. Many more reactions are necessary for a biological implementation than for a simple chemical implementation, as the activator and inhibitor do not directly interact. Rather, the system in Figure S1a must be implemented through several signal-protein, protein-protein, and protein-DNA interactions. Due to the number of reactions and of different design variations possible, computational modeling is critical for guiding the translation of the abstract design in Figure S1a into a genetic network.

As a starting point, we explored the genetic network design shown in Figure S1b. In this system, $A_{3OC12HSL}$ binds LasR and activates two different p(Las)-OR1 promoters that express *lasI* and *rhlI*. Since LasI catalyzes $A_{3OC12HSL}$ synthesis, $A_{3OC12HSL}$ is effectively autocatalytic. Similarly, since RhlI catalyzes synthesis of I_{C4HSL}, the $A_{3OC12HSL}$ activator also activates the I_{C4HSL} inhibitor. I_{C4HSL} binds RhlR and activates the p(Rhl) promoter, which expresses the λ phage CI repressor. CI represses the two p(Las)-OR1 promoters and thus inhibits further production of $A_{3OC12HSL}$ and I_{C4HSL}. CI also represses the p(Rhl)-OR1 promoter. We developed a detailed model of this system and confirmed through linear stability analysis that Turing instabilities could be achieved for certain parameter sets, and also confirmed through spatial simulations that patterns could form (6).

We then proceeded to consider design modifications that could potentially result in more robust patterning. One of the overall design goals was to create a network enriched for Turing instabilities but simple enough to physically construct and tune. In order to increase the chances of finding parameter sets with Turing instabilities without making the system much more complex, we developed code to perform stability analysis on random parameter sets for different design variations. As shown in Figure S2a, these alternative implementations had CI OR1 binding domains in different combinations of promoters, and some expressed a $A_{3OC12HSL}$ degrading acylase from the p(Rhl) promoter (7). Equations 1-27 were used to model the design variations, and kinetic rates were chosen according to Tables S1-S3. This model explicitly captures production and decay of mRNA, production and decay of proteins, and binding and dissociation of AHL and R-proteins. However, quasi steady state approximations were used for protein-DNA interactions. As found by other synthetic biology studies (8), detailed models of this nature can be important for capturing delays that impact system function.

www.pnas.org/cgi/doi/10.1073/pnas.1720770115

$$\frac{\partial mrnalasr}{\partial t} = k_{XSCRIBE\_LASR} * PCOPY * hill\_ci\_lasr - k_{DEC\_MRNA} * mrnalasr \quad [1]$$

$$\frac{\partial mrnarhli}{\partial t} = k_{XSCRIBE\_QSCLAS1} * PCOPY * hill\_activ\_qsclas1 * hill\_ci\_qsclas1 - k_{DEC\_MRNA} * mrnarhli \quad [2]$$

$$\frac{\partial lasr}{\partial t} = k_{XLATE\_LASR} * mrnalasr - k_{BIND\_LASR\_A} * lasr * A + k_{DIS\_LASR\_A} * lasr\_A - k_{DEC\_LASR} * lasr \quad [3]$$

$$\frac{\partial rhli}{\partial t} = k_{XLATE\_RHLI} * mrnarhli - k_{DEC\_RHLI} * rhli \quad [4]$$

$$\frac{\partial lasr\_A}{\partial t} = k_{BIND\_LASR\_A} * lasr * A - k_{DIS\_LASR\_A} * lasr\_A - k_{DEC\_LASR\_A} * lasr\_A \quad [5]$$

$$\frac{\partial A}{\partial t} = k_{SYNTH\_A} * lasi - k_{BIND\_LASR\_A} * lasr * A + k_{DIS\_LASR\_A} * lasr\_A - k_{BIND\_RHLR\_A} * rhlr * A + k_{DIS\_RHLR\_A} * rhlr\_A - k_{BIND\_ACYLASE} * acylase * A - k_{DEC\_A} * A + k_{DIFFUSE\_A} * \nabla^2 A \quad [6]$$

$$\frac{\partial I}{\partial t} = k_{SYNTH\_I} * rhli - k_{BIND\_RHLR\_I} * rhlr * I + k_{DIS\_RHLR\_I} * rhlr\_I - k_{DEC\_I} * I + k_{DIFFUSE\_I} \nabla^2 I \quad [7]$$

$$\frac{\partial mrnarhlr}{\partial t} = k_{XSCRIBE\_RHLR} * PCOPY * hill\_ci\_rhlr - k_{DEC\_MRNA} * mrnarhlr \quad [8]$$

$$\frac{\partial mrnaci}{\partial t} = k_{XSCRIBE\_QSCRHL} * PCOPY * hill\_activ\_qscrhl * hill\_ci\_qscrhl - k_{DEC\_MRNA} * mrnaci \quad [9]$$

$$\frac{\partial rhlr}{\partial t} = k_{XLATE\_RHLR} * mrnarhlr$$

$$
\begin{aligned}
&- k_{BIND\_RHLR\_I} * rhlr * I \\
&+ k_{DIS\_RHLR\_I} * rhlr\_I \\
&- k_{BIND\_RHLR\_A} * rhlr * A \\
&+ k_{DIS\_RHLR\_A} * rhlr\_A \\
&- k_{DEC\_RHLR} * rhlr
\end{aligned} \quad [10]
$$

$$
\begin{aligned}
\frac{\partial ci}{\partial t} &= k_{XLATE\_CI} * mrnaci \\
&- k_{DEC\_CI} * ci
\end{aligned} \quad [11]
$$

$$
\begin{aligned}
\frac{\partial rhlr\_I}{\partial t} &= k_{BIND\_RHLR\_I} * rhlr * I \\
&- k_{DIS\_RHLR\_I} * rhlr\_I \\
&- k_{DEC\_RHLR\_I} * rhlr\_I
\end{aligned} \quad [12]
$$

$$
\begin{aligned}
\frac{\partial mrnalasi}{\partial t} &= k_{XSCRIBE\_QSCLAS2} * PCOPY * hill\_activ\_qsclas2 * hill\_ci\_qsclas2 \\
&- k_{DEC\_MRNA} * mrnalasi
\end{aligned} \quad [13]
$$

$$
\begin{aligned}
\frac{\partial lasi}{\partial t} &= k_{XLATE\_LASI} * mrnalasi \\
&- k_{DEC\_LASI} * lasi
\end{aligned} \quad [14]
$$

$$
\begin{aligned}
\frac{\partial mrnaacylase}{\partial t} &= k_{XSCRIBE\_QSCRHL2} * PCOPY * hill\_activ\_qscrhl2 * hill\_ci\_qscrhl2 \\
&- k_{DEC\_MRNA} * mrnacylase
\end{aligned} \quad [15]
$$

$$
\begin{aligned}
\frac{\partial acylase}{\partial t} &= k_{XLATE\_ACYLASE} * mrnaacylase \\
&- k_{DEC\_acylase} * acylase
\end{aligned} \quad [16]
$$

$$
\begin{aligned}
\frac{\partial rhlr\_A}{\partial t} &= k_{BIND\_RHLR\_A} * rhlr * A \\
&- k_{DIS\_RHLR\_A} * rhlr\_A
\end{aligned} \quad [17]
$$

$$
hill\_ci\_lasr = 1 - \frac{ci^2}{ci^2 + k^2_{HALFMAX\_CI\_LASR}} \quad [18]
$$

$$
hill\_ci\_rhlr = 1 - \frac{ci^2}{ci^2 + k^2_{HALFMAX\_CI\_RHLR}} \quad [19]
$$

$$
hill\_activ\_qsclas1 = \frac{lasr\_A^2}{lasr\_A^2 + k^2_{HALFMAX\_LAS}} + k_{BASAL\_QSCLAS1} \quad [20]
$$

$$
hill\_ci\_qsclas1 = 1 - \frac{ci^2}{ci^2 + k^2_{HALFMAX\_CI\_QSCLAS1}} \quad [21]
$$

$$
hill\_activ\_qscrhl = \frac{rhlr\_I^2}{rhlr\_I^2 + k^2_{HALFMAX\_RHL}} + k_{BASAL\_QSCRHL} \quad [22]
$$

$$
hill\_activ\_qscrhl2 = \frac{rhlr\_I^2}{rhlr\_I^2 + k^2_{HALFMAX\_RHL2}} + k_{BASAL\_QSCRHL2} \quad [23]
$$

$$
hill\_ci\_qscrhl = 1 - \frac{ci^2}{ci^2 + k^2_{HALFMAX\_CI\_QSCRHL}} \quad [24]
$$

Table S1. Kinetic constants used for exploring design variations depicted in Figure S2a. Las promoter 1 is the promoter expressing *rhlI*, while Las promoter 2 refers to a separate Las promoter expressing *lasI*. Rhl promoter 1 is the promoter expressing *cI*, while Rhl promoter 2 refers to a separate Rhl promoter expressing *acylase*. $RAND(a,b)$ is a number randomly selected from the uniform interval [a,b], and bit_n is the n^{th} bit of the binary representation of the network number. Tables S2-S3 contain the rest of the parameters for this system.

$k_{XSCRIBE\_RHLR}$	transcription rate of *rhlR*	0.025 μM·hs^{-1}
$k_{XSCRIBE\_LASR}$	transcription rate of *lasR*	0.025 μM·hs^{-1}
$k_{XSCRIBE\_QSCRHL}$	Rhl promoter transcription rate	0.025 μM·hs^{-1}
$k_{XSCRIBE\_QSCLAS1}$	activated Las promoter 1 transcription rate	0.025 μM·hs^{-1}
$k_{XSCRIBE\_QSCLAS2}$	activated Las promoter 2 transcription rate	0.025 μM·hs^{-1}
k_{BASAL_QSCRHL}	basal transcription rate for Rhl promoter 1	0.001 μM·hs^{-1}
$k_{BASAL\_QSCRHL2}$	basal transcription rate for Rhl promoter 2	0.001 μM·hs^{-1}
$k_{BASAL\_QSCLAS1}$	basal transcription rate for Las promoter 1	0.001 μM·hs^{-1}
$k_{BASAL\_QSCLAS2}$	basal transcription rate for Las promoter 2	0.001 μM·hs^{-1}
k_{XLATE_RHLR}	translation rate of RhlR	$RAND(0.25,25)$ hs^{-1}
k_{XLATE_LASR}	translation rate of LasR	$RAND(0.25,25)$ hs^{-1}
k_{XLATE_CI}	translation rate of CI	$RAND(0.25,25)$ hs^{-1}
k_{XLATE_LASI}	translation rate of LasI	$RAND(0.25,25)$ hs^{-1}
k_{XLATE_RHLI}	translation rate of RhlR	$RAND(0.25,25)$ hs^{-1}
$k_{XLATE\_ACYLASE}$	translation rate of acylase	$bit_6 \cdot RAND(0.25,25)$ hs^{-1}
$k_{HALFMAX\_RHL}$	Concentration of RhlR/I complex giving half-maximal Rhl promoter 1 activation	1 μM
$k_{HALFMAX\_RHL2}$	Concentration of RhlR/I complex giving half-maximal Rhl promoter 2 activation	1 μM
$k_{HALFMAX\_LAS}$	Concentration of LasR/A complex giving half-maximal Las promoter activation	0.01 μM

$$hill\_ci\_qscrhl2 = 1 - \frac{ci^2}{ci^2 + k^2_{HALFMAX\_CI\_QSCRHL2}} \quad [25]$$

$$hill\_activ\_qsclas2 = \frac{lasr\_A^2}{lasr\_A^2 + k^2_{HALFMAX\_LAS}} + k_{BASAL\_QSCLAS2} \quad [26]$$

$$hill\_ci\_qsclas2 = 1 - \frac{ci^2}{ci^2 + k^2_{HALFMAX\_CI\_QSCLAS2}} \quad [27]$$

In the simulations, each different implementation corresponded to a certain network number. A promoter contained an OR1 domain if the corresponding bit in the binary representation of the network number was a 1 (Figure S2a). Likewise, acylase was expressed only if bit_6 of the binary representation of the network number was 1. For example, $56_{10} = 0111000_2$, so Network 56 has an OR1 site in the p(Las)-OR1 promoters expressing LasI and RhlI and in the promoter expressing RhlR since bit_3, bit_4, and bit_5 are all 1. Figure S2b shows the number of parameter sets with Turing instabilities found for each different network. Although Network 106 was most enriched for Turing instabilities, this network requires acylase expression. Networks 56 and 57, depicted in Figure S1c, do not require acylase expression and were ultimately chosen instead for the sake of simplicity.

Having chosen a network architecture, we then investigated the role of key parameters in determining the existance of Turing instabilities(6). Of particular importance, we found that sensitive responses of the p(Las)-OR1 promoter were important for achieving Turing instabilities. Since the results suggested that the Hill coefficient of p(Las) activation must be greater than 1 for pattern formation, we

Table S2. Kinetic constants used for exploring design variations, continued from Table S1. The remaining constants are in Table S3.

$k_{HALFMAX\_CI\_QSCLAS1}$	Concentration of CI giving half-maximal Las promoter 1 repression	$RAND(0.007796, 0.7796)/bit_5$ μM
$k_{HALFMAX\_CI\_QSCLAS2}$	Concentration of CI giving half-maximal Las promoter 2 repression	$RAND(0.007796, 0.7796)/bit_4$ μM
$k_{HALFMAX\_CI\_QSCRHL}$	Concentration of CI giving half-maximal Rhl promoter 1 repression	$RAND(0.007796, 0.7796)/bit_3$ μM
$k_{HALFMAX\_CI\_QSCRHL2}$	Concentration of CI giving half-maximal Rhl promoter 2 repression	$RAND(0.007796, 0.7796)/bit_0$ μM
$k_{HALFMAX\_CI\_RHLR}$	Concentration of CI giving half-maximal repression of RhlR	$RAND(0.007796, 0.7796)/bit_3$ μM
$k_{HALFMAX\_CI\_LASR}$	Concentration of CI giving half-maximal repression of LasR	$RAND(0.007796, 0.7796)/bit_1$ μM
k_{DEC_RHLR}	decay rate of RhlR	0.029 hs^{-1}
k_{DEC_LASR}	decay rate of LasR	0.029 hs^{-1}
k_{DEC_CI}	decay rate of CI	0.116 hs^{-1}
k_{DEC_LASI}	decay rate of LasI	0.116 hs^{-1}
k_{DEC_RHLI}	decay rate of RhlI	0.116 hs^{-1}
$k_{DEC\_ACYLASE}$	decay rate of acylase	0.116 hs^{-1}
k_{DEC_MRNA}	decay rate of mRNA	1.16 hs^{-1}
k_{DEC_I}	decay rate of I_{C4HSL}	0.002 hs^{-1}
k_{DEC_A}	decay rate of $A_{3OC12HSL}$	0.002 hs^{-1}
$k_{DEC\_RHLR\_I}$	decay rate of RhlR/I_{C4HSL} complex	0.029 hs^{-1}
$k_{DEC\_LASR\_A}$	decay rate of LasR/$A_{3OC12HSL}$ complex	0.029 hs^{-1}

Table S3. Kinetic constants used for exploring design variations, continued from Tables S1-S2.

D_I	I_{C4HSL} diffusion rate	0.003 gridpoints$^2 \cdot hs^{-1}$
D_A	$A_{3OC12HSL}$ diffusion rate	0.0003 gridpoints$^2 \cdot hs^{-1}$
$k_{BIND\_RHLR\_I}$	binding rate of RhlR and I_{C4HSL}	0.1 $\mu M^{-1} hs^{-1}$
$k_{BIND\_RHLR\_A}$	binding rate of RhlR and $A_{3OC12HSL}$	0.1 $\mu M^{-1} hs^{-1}$
$k_{BIND\_LASR\_A}$	binding rate of LasR and $A_{3OC12HSL}$	0.1 $\mu M^{-1} hs^{-1}$
$k_{BIND\_ACYLASE}$	destruction rate of $A_{3OC12HSL}$ by acylase	0.0023 $\mu M^{-1} hs^{-1}$
$k_{DIS\_RHLR\_I}$	dissociation of RhlR/I_{C4HSL} complex	1 hs^{-1}
$k_{DIS\_RHLR\_A}$	dissociation of RhlR/$A_{3OC12HSL}$ complex	1 hs^{-1}
$k_{DIS\_LASR\_A}$	dissociation of LasR/$A_{3OC12HSL}$ complex	1 hs^{-1}
k_{SYNTH_I}	synthesis rate of I_{C4HSL} (9)	0.5 hs^{-1}
k_{SYNTH_A}	synthesis rate of $A_{3OC12HSL}$ (9)	0.5 hs^{-1}
PCOPY	Plasmid copy number	10

considered placing LasR under the control of a p(Las)-OR1 promoter. Starting even with a p(Las) promoter that responds hyperbolically to $A_{3OC12HSL}$ (Hill coefficient of 1), an ultrasensitive reporter response can be engineered by placing *lasR* under control of the p(Las) promoter. This can be demonstrated as follows. Suppose a p(Las) promoter regulates both LasR and a reporter. It can be assumed that the steady state reporter level is proportional to the steady state LasR level. The differential equation for LasR is given in Equation 28.

$$\frac{\partial L}{\partial t} = \frac{\alpha_0 + \alpha_1 (KSL)^m}{1 + (KSL)^m} - dL \quad [28]$$

Here, α_0 is the basal expression rate and α_1 is the maximum rate of expression from the activated promoter. K is the inverse of the level of $A_{3OC12HSL}$/LasR that gives rise to promoter expression at a rate that is halfway between basal and maximal expression. S is the $A_{3OC12HSL}$ signal, d is the LasR decay rate, and m is the Hill coefficient of p(Las) activation by $A_{3OC12HSL}$/LasR.

One commonly used metric for measuring sensitivity is the cooperativity index R_C (10, 11), defined for this system as the ratio of S necessary for 90% promoter activation to S necessary for 10% promoter activation. This corresponds to Equations 29-33.

$$L_{90} = 0.1\alpha_0 + 0.9\alpha_1 \quad [29]$$

$$L_{10} = 0.9\alpha_0 + 0.1\alpha_1 \quad [30]$$

$$S_{90} = \frac{1}{KL_{90}} \sqrt[m]{\frac{dL_{90} - \alpha_0}{\alpha_1 - dL_{90}}} \quad [31]$$

$$S_{10} = \frac{1}{KL_{10}} \sqrt[m]{\frac{dL_{10} - \alpha_0}{\alpha_1 - dL_{10}}} \quad [32]$$

$$R_C = \frac{S_{90}}{S_{10}} \quad [33]$$

For a p(Las) promoter that has a Hill coefficient of 1 when LasR is constitutively expressed, L is given by Equation 34, and the cooperativity index is given by Equation 35. For $\alpha_1 \gg \alpha_0$, the cooperativity index is almost 9. Although Equation 34 is not a Hill equation, a cooperativity index of 9 would correspond to a Hill coefficient of 2. Figure S3 illustrates the enhancement in sensitivity gained by placing LasR under control of p(Las). Reporter output versus $A_{3OC12HSL}$ is shown for constitutive LasR expression and for LasR under control of p(Las) using the following parameter set: $\alpha_0 = 0.01$, $\alpha_1 = 1$, $K = 0.5$, $d = 1$, $m = 1$.

$$L = \frac{\alpha_1 KS - d + \sqrt{(\alpha_1 KS - d)^2 + 4dK\alpha_0 S}}{2dKS} \quad [34]$$

$$R_C = \frac{81(9\alpha_0 + \alpha_1)}{\alpha_0 + 9\alpha_1} \quad [35]$$

Equation 34 was used to represent reporter concentration for the case of LasR under control of p(Las). This was done because the steady state reporter level is proportional to the level of LasR, as mentioned previously. For the case of constitutive LasR expression, the Equation 36 was used to represent steady state reporter concentration.

$$reporter_{LasRconstit} = \frac{\alpha_0 + \alpha_1 \frac{K\alpha_1 S}{d}^m}{d(1 + \frac{K\alpha_1 S}{d}^m)} \quad [36]$$

Having modified our design to incorporate positive feedback on LasR, we arrived at the final design shown in Fig. S1c and Fig. 1 of the main text. We then proceeded to construct the system in a modular fashion.

2. System construction

Each genetic part for our system was characterized prior to assembly into devices. Table S4 describes provides references to characterizations of the constructs used for this study. For many of these components, standardized BioBrick components are available. Devices were assembled from these genetic parts in a modular fashion (6). We now describe the DNA constructs for our final system.

Table S4. Sources of genetic parts.

Genetic Part	References
lasI(LVA)	(6, 12), BBa_C0078
rhlI	(6, 12), BBa_C0170
lasR	(6, 12), BBa_C0179
rhlR-I124F	(6)
cI(LVA)	(13–15), BBa_C0051
lacI	BBa_I732100
GFP(LVA)	(16), BBa_K082003
DsRed-Express	Clontech
$\lambda_{P(R-O1)}$	(6)
pLas-OR1	(6), BBa_I14016
pRhl-LacO	this study

A. Plasmid Construction. Our patterning circuit design was implemented by partitioning the system into two plasmids, namely pFNK-512 (Fig. S4a) and pFNK-804-LacO-LacI (Fig. S4b), corresponding to the upper and lower parts of the circuit diagram in Fig. 1b of the main text. pFNK-512 was constructed by inserting two identical divergent copies of the hybrid promoter $P_{Las-OR1}$ as well as the genes *lasI(LVA)*, *rhlI*, *dsRed*, and *lasR* into the pPROTet.E vector (ColE1 ori and Cm resistance, Clontech). The promoter $P_{Las-OR1}$ was constructed by fusing a mutant CI binding domain O_{R1}-mut4 (17) to a wildtype Las promoter in *P. aeruginosa* (PAO1 strain) (6, 18). The hybrid promoter sequence is shown in Fig. S4g. This approach for constructing promoters that are activated by quorum sensing signals, yet repressed by repressors such as cI has been previously described (13). A Las regulatory gene *lasR* was placed downstream of one copy of the hybrid promoter. $A_{3OC12HSL}$ and I_{C4HSL} synthase genes *lasI(LVA)* and *rhlI* were inserted downstream of the other $P_{Las-OR1}$ promoter followed by a red fluorescence reporter gene *dsRed-exp* (from Clontech plasmid pDsRed-Exp). RBSII was used for all ribosome binding sites in this plasmid (17).

pFNK-804-LacO-LacI was constructed starting from the pPROLar.A vector (ColE1 ori and Kan resistance, Clontech) and integrating the promoters p_{LacIq}, $\lambda_{P(R-O1)}$, and $P_{Rhl-lacO}$ and the genes *lacI*, *rhlR*, *cI*, and *GFP(LVA)* (19). The constitutive promoter p_{LacIq}, ribosome binding site RBSII, and *lacI* gene were inserted into the vector for constitutive expression of LacI (17). A mutant *rhlR* (6) was placed under control of a CI-regulated promoter $\lambda_{P(R-O1)}$ and the ribosome binding site RBSH (6, 18, 19). The *rhlR* mutant, *RhlR-I124F* was selected by directed evolution for its response to lower concentrations of I_{C4HSL} than the wildtype (6). Hybrid promoter $P_{Rhl-lacO}$ was constructed by adding a LacO operator binding site to a wildtype RhlR promoter in *P. aeruginosa* (Fig. S4g). Genes *cI* and *GFP(LVA)* were placed under transcriptional control of the hybrid promoter $P_{Rhl-lacO}$. Ribosome binding sites RBSH and RBSII were used for *cI* and *GFP* respectively (17, 19).

Plasmid pFNK-806 (Fig. S4c) was derived from pFNK-804-LacO-LacI. It was constructed by replacing promoter $\lambda_{P(R-O1)}$ in pFNK-804-LacO-LacI with the constitutive promoter p_{LacIq}, and replacing the corresponding ribosome binding site RBSII with RBSG (17). This provided a plasmid without the inhibition of RhlR production by CI.

Plasmid pTOG-1 (Fig. S4d was created from toggle switch plasmid pIKE-107 (ColE1 ori and Amp resistance) (20). We inserted a red fluorescence gene *mCherry* into the original plasmid downstream of the *lacI* gene that is regulated by promoter $p_{LtetO-1}$. RBSII was used as the ribosome binding site for *mCherry* (17).

Plasmids pINV-5 and pASK-201 were used for the negative controls in Fig. 2b in the main text. The pINV-5 plasmid expresses *lacI* from the constitutive promoter p_{LacIq} and expresses *GFP(LVA)* from the LacI-regulated promoter p_{Lac} on a p15A plasmid with

kanamycin resistance (Fig. S4e) (21). Plasmid pASK-201 is identical to pINV-5 except that *gfp(lva)* was replaced by a red fluorescence gene *dsRed-Exp* (Fig. S4f).

All plasmids were constructed using standard molecular biology cloning techniques. Restriction enzymes were obtained from New England BioLabs Inc, and PCR primers were ordered from Integrated DNA Technologies, Inc.

3. Diffusion experiments and mathematical modeling

A requirement for Turing pattern formation is two morphogens that have distinct diffusion rates. Specifically, the activator species $A_{3OC12HSL}$ should diffuse more slowly than the inhibitor I_{C4HSL}. To quantify the difference between the diffusion rates, we performed dosage response experiments, solid-phase diffusion experiments, mathematical modeling, and parameter estimation.

AHL response threshold. To conduct the diffusion assays, we first needed to calibrate the morphogen response thresholds. We individually transformed plasmids pFNK202-qsc119 and pFNK503-qscrsaL into strain MG1655 to serve as reporter cells for I_{C4HSL} and $A_{3OC12HSL}$ respectively (12). pFNK202-qsc119 is a I_{C4HSL} reporter construct that expresses RhlR constitutively and expresses a GFP(LVA) reporter from the p(Rhl) promoter. pFNK503-qscrsaL is a $A_{3OC12HSL}$ reporter construct that expresses LasR constitutively and expresses a GFP(LVA) reporter from the p(Las) promoter (12). Reporter cells inoculated from overnight cultures were grown in M9 media for 3 hours and then induced with various levels of AHL for 6 hours. Single cell fluorescence data were subsequently collected using a Beckman Coulter Altra flow cytometer equipped with a 488-nm argon excitation laser and a 515-545 nm emission filter. Figure S5 shows the dosage response curves for I_{C4HSL} and $A_{3OC12HSL}$ receiver cells. The half activation thresholds are approximately 3×10^{-3} µM for $A_{3OC12HSL}$ and 3 µM for I_{C4HSL}. This information allows us to correlate fluorescence activation with AHL concentration in our solid-phase diffusion experiments.

Diffusion experiments. We performed solid-phase diffusion experiments in 2% M9 agar plates as described in Methods. Reporter cells picked from single colonies were cultured in liquid LB media overnight and diluted 1000:1 into fresh media the next day. When culture OD's reached $0.1 - 0.3$, cells were concentrated and resuspended in M9 media to final OD of 2.0. 1.5 mL of the concentrated cells were plated onto 80×15 mm M9 agar Petri dishes for the diffusion experiments. To correspond with the environmental conditions of our patterning experiments, plates with the cells were first incubated at 30 ^{o}C for 12 hours. Afterwards, 3 μL AHL droplets with an appropriate concentration (10 mM for I_{C4HSL}, and 0.01 mM for $A_{3OC12HSL}$) were added at the center of the plates for each type of reporter cell. We chose these concentrations based on the AHL's half activation thresholds so that the AHL's activate cells around the center but not close to the edge of the Petri dishes. Fluorescence images were taken at hours 0, 2.5, 5, and 8.75 using a Bio-rad Molecular Imager ChemiDoc XRS+ System. An XcitaBlue conversion screen was used for capturing GFP intensities.

Every image obtained from this experiment has a fluorescence radial gradient centered around the position where the AHL droplet was added. Figure S6a-b shows representative fluorescence intensity lines crossing the image centers for different time points for the two AHL diffusion experiments. The image exposure times for I_{C4HSL} and $A_{3OC12HSL}$ are 0.1 s and 0.2 s respectively. Raw images were processed to remove exposure bias in the field of view by background subtraction of reference frames.

We then conducted experiments to ensure that the diffusion of I_{C4HSL} and $A_{3OC12HSL}$ did not drastically change due to potential differences in biofilm characteristics over many hours of incubation. Specifically, the diffusion experiment was again carried out, varying the initial incubation time before AHL addition. Images were then captured following 0, 2.5, 5, and 8 hours of AHL exposure (Fig. S7).

Modeling and parameter estimation. To estimate experimental diffusion coefficients for the signaling species, we developed the following reaction-diffusion model:

$$\frac{\partial S}{\partial t} = D_s \nabla^2 S - \gamma_s S \quad [37]$$

$$\frac{\partial F}{\partial t} = \alpha_f N \frac{S}{K_s + S} - \gamma_f F \quad [38]$$

$$\frac{\partial N}{\partial t} = \alpha_n N(1 - N/N_l) \quad [39]$$

This model captures the behavior of the reporter cells harboring reporter constructs pFNK202-qsc119 and pFNK503-qscrsaL. In this model, S, F, and N refer to AHL concentration, fluorescence reporter concentration, and cell density respectively. γ_s and γ_f are the degradation rates for AHL and the fluorescence reporter, D_s is the AHL diffusion coefficient, K_s is the AHL half-activation threshold, α_f is the fluorescence reporter production rate and α_n is the cell growth rate. In this model, cell density is assumed to grow logistically (22).

According to our experimental setup, the initial conditions of the equations include $F(x,t)|_{t=0} = 0$, $N(x,t)|_{t=0} = N_0$ and $S(x,t)|_{t=0} = S_0 \mathrm{H}[x+x_0](1-\mathrm{H}[x-x_0])$, where $\mathrm{H}[x]$ is the Heaviside step function and x_0 is the radius of the initial AHL droplet. The signal's initial condition was chosen as above to simulate the localized addition of AHL droplets onto the plate. The boundary conditions of the system are $\partial S/\partial x|_{x=\pm 4} = 0$, $\partial F/\partial x|_{x=\pm 4} = 0$, and $\partial N/\partial x|_{x=\pm 4} = 0$. Since the fluorescence observed in our experiment consists of the fluorescence reporter and cell autofluorescence, the total fluorescence is indicated by $F_{total} = F + \beta_f N$.

From the literature (23), we use degradation rates of $\gamma_{s=c_{12}} = 0.002$ hr^{-1} for $\mathrm{A_{3OC12HSL}}$ and $\gamma_{s=c_4} = 0.02$ hr^{-1} for $\mathrm{I_{C4HSL}}$. The degradation rate of the fluorescent protein is $\gamma_f = 0.04$ hr^{-1}. We choose $\beta_f = 0.5$ for $\mathrm{I_{C4HSL}}$ (0.1 s exposure time) and $\beta_f = 1.0$ for $\mathrm{A_{3OC12HSL}}$ (0.2 s exposure time). From the dosage response experiment, we obtained half activation thresholds for the two AHLs of $K_{s=c_{12}} = 0.003$ μM and $K_{s=c_4} = 3$ μM. By parameter estimation using the fluorescence intensities of cells far away from the center in the model with the experimental setup, we obtained a cellular growth rate of $\alpha_n = 0.15$ hr^{-1} and saturation cell density of $N_l = 5.0$ ($N_0 = 1.0$). Then, by parameter estimation of the fluorescence wave profile over time, we estimate the diffusion coefficients to be $D_{c_{12}} = 0.003$ cm^2/hr for $\mathrm{A_{3OC12HSL}}$ and $D_{c_4} = 0.065$ cm^2/hr for $\mathrm{I_{C4HSL}}$. The corresponding simulation results are shown in Fig. S6c-d. These experiments suggest that the diffusion coefficient for the activator is approximately 21.6 fold slower than that of the inhibitor, qualitatively consistent with a previous study (24). One possible explanation for why the ratio of diffusion rates is higher than expected based on molecular weight differences alone is that the hydrophobic nature of $\mathrm{A_{3OC12HSL}}$ causes it to partition in the cell membrane, thus essentially slowing down its diffusion from cell to cell (24).

4. Signal Specificity and Competitive Inhibition

An initial design challenge was to identify sufficiently non-interacting cell-cell signaling systems. Our choice of harnessing the *Pseudomonas aeruginosa* Rhl and Las quorum sensing systems was based on the potential for achieving specific responses to two different signals in the same cell (3). In *P. aeruginosa*, $\mathrm{A_{3OC12HSL}}$ and $\mathrm{I_{C4HSL}}$ are the two signaling molecules of the Las and Rhl quorum sensing pathways: $\mathrm{A_{3OC12HSL}}$ and LasR are responsible for activation of the $\mathrm{p_{Las}}$ promoter while $\mathrm{I_{C4HSL}}$ and RhlR regulate the $\mathrm{p_{Rhl}}$ promoter. Many promoters in *P. aeruginosa* are quorum sensing controlled and exhibit varying degrees of specificity to $\mathrm{A_{3OC12HSL}}$ and/or $\mathrm{I_{C4HSL}}$. Therefore, we first identified a Rhl promoter, the rhlAB promoter, that specifically responded to $\mathrm{I_{C4HSL}}$/RhlR and a Las promoter, the rsaL promoter, that specifically responded $\mathrm{A_{3OC12HSL}}$/LasR (6). As an example demonstration of signal specificity, we used *E. coli* cells that harbor a plasmid (pFNK202-qsc119) with constitutively expressed RhlR and a $\mathrm{p_{Rhl}}$ promoter regulating a GFP(LVA) reporter (12). We performed crosstalk experiments by inducing the engineered cells with different combinations of the AHLs. Our experiments along with previous results (12) confirm that the Rhl pathway is activated by $\mathrm{I_{C4HSL}}$ but not by $\mathrm{A_{3OC12HSL}}$ in the presence of RhlR (Fig. S8a).

In spite of the specific response of our Las and Rhl promoters to $\mathrm{A_{3OC12HSL}}$/LasR and $\mathrm{I_{C4HSL}}$/RhlR, an important interaction still exists. Namely, $\mathrm{A_{3OC12HSL}}$ can competitively bind RhlR. To explore the effects of this competitive binding, we induced *rhl* receiver cells with different levels of $\mathrm{A_{3OC12HSL}}$ (0 to 30 μM) while $\mathrm{I_{C4HSL}}$ was kept high (3 μM). Figure S8b shows that the fluorescence level of single cells monotonically decreases with $\mathrm{A_{3OC12HSL}}$. This experiment suggests that $\mathrm{A_{3OC12HSL}}$ binds RhlR, the regulatory protein for $\mathrm{I_{C4HSL}}$, but the corresponding complex does not activate the promoter $\mathrm{p_{Rhl}}$. The competitive binding of $\mathrm{A_{3OC12HSL}}$ to RhlR thus reduces RhlR/$\mathrm{I_{C4HSL}}$ complex formation and, as a result, inhibits $\mathrm{p_{Rhl}}$ activation from $\mathrm{I_{C4HSL}}$. In wildtype *P. aeruginosa*, this competitive inhibition may provide an alternative mechanism for temporal control of the activation of transcription factors by delaying the induction

of genes regulated by the *rhl* quorum sensing pathway (25). In our system, this inhibition attenuates GFP in the red fluorescent activator regions.

5. Control Experiments and Pattern Characteristics

To demonstrate that our system exhibits stochastic Turing patterns, we showed that our patterns are not a result of the outward growth of clusters of differentially colored cells. For this we first assayed the phenotypic behavior of lawns of cells that express fluorescent proteins constitutively. As shown in Fig. 2b, when red and green fluorescent cells are grown separately or together, uniform fluorescent fields develop. The difference between these control experiments and the emergent patterns is illustrated clearly in the red/green fluorescence density plots (Fig. 2c). We further tested additional ratios of constitutively fluorescent green and red cells and again observed relatively uniform fields of fluorescence (Fig. S9). These experiments demonstrate that, in our experimental setup, neither cell growth nor initial spatial heterogeneity of cell density give rise to the large scale spatial patterns observed with the Turing cells.

Next, we tested whether observable patterns would emerge if individual cells autonomously made cell-fate decisions at some point after plating. This would indicate that our system is not, in fact, generating emergent patterns. To address this question, we performed another experiment with cells that harbor independent bistable green/red toggle switches (Fig. S10a) (20). For these switches, which are essentially net positive feedback loops, IPTG induction results in expression of TetR/GFP, aTc induction results in expression of LacI/RFP, and absence of inducer results in a 'memory' of the cells' most recent state (at 30^{o}C) (20). Co-induction with both inducers gives rise to co-expression of all proteins; subsequent simultaneous removal of the inducers causes each cell to make an independent quasi-random decision and enter one of the two stable states. To explore whether such an independent decision-making process results in global pattern formation, we induced toggle cells with 3 μM IPTG and 0.3 μM aTc in liquid culture for 5 hours. Flow cytometry analysis confirmed that after this initial incubation period, all cells in the population had roughly the same red/green fluorescence levels (Fig. S10b). Co-induced cells were then plated onto Petri dishes lacking inducers (bistability condition) using the same technique as the experiments above. The fluorescence fields after 24 hour incubation at 30 ^{o}C were uniform, showing no emergence of patterns (Fig. S10d-f). However, flow cytometry analysis of cells scraped from the plate after 24 hours revealed that the initially homogeneous cell population had bifurcated almost completely into two subpopulations, one with high GFP expression and the other with high RFP expression (Fig. S10c). The toggle switch cell lawn maintained spatial homogeneity but individual cells settled into one of the two states, suggesting that this autonomous quasi-random fate decision by individual cells does not lead to global spatial patterning.

Next we explored the robustness and structural stability of our results: specifically, whether and how changes in the levels of localized interactions lead to different global outcomes. In our system, IPTG can be used to modulate the inhibitory efficiency of I_{C4HSL} in individual cells by affecting CI expression from $P_{Rhl-lacO}$, up to the threshold of toxicity. Our data show that mean GFP levels increase sigmoidally with inducer concentration while the overall area of red spots decreases (Fig. 3b-c), correlating well with the results from our mathematical model (Fig. 3d-g). To quantify changes in the spatial characteristics of the patterns in response to different IPTG concentrations, we define a *collectivity metric* as follows:

$$\Theta = \sum_{i,j=1}^{M} \sigma_{i,j}, \quad \text{where } \sigma_{i,j} = \begin{cases} 1 & \text{if pixels } i \text{ and } j \text{ are in the same red spot} \\ 0 & \text{otherwise} \end{cases}$$

where M is the total number of pixels in the image. Fig. 3b shows that in our experiments, the collectivity metric decreases approximately 9 fold as a function of IPTG, indicating that an increase in the inhibitory effect of I_{C4HSL} in each individual cell results in reduced overall global clustering. Moran's I (26) is also plotted to illustrate how the spatial autocorrelation of an image decreases with IPTG (Fig. 3b, inset), qualitatively consistent with the analysis of our simulated patterns (Supplementary Information, Fig. S11).Additionally, spots become smaller due to IPTG induction as is visible in the microscope images in Fig. 3a.

We performed a 32-hour experiment to gain a better understanding of the dynamics of pattern emergence. A lawn of cells was prepared as described in Methods, placed in a microscope chamber and incubated at 30 ^{o}C. Fluorescence images of the same region

were captured once every 30 minutes. Figure S12 shows images at 4 hour intervals (0-, 4-, 8-, 12-, 16-, 20-, 24-, 28-, and 32-hour). There is no fluorescence initially until hour 16 when tiny spots emerge. These tiny spots grow quickly and new spots continue appearing and growing during the following few hours. By hour 24, spots have emerged with typical sizes much larger than that of a single cell. The spot pattern remains roughly the same from hour 24 to hour 32. However, as our experimental system is fundamentally a dissipative system, and we do not feed fresh nutrients, an eventual breakdown is inevitable.

We can also extract the characteristic scale of the pattern. To do this we found the centroid points of each clump of activator. We then created a histogram of distances to to nearest neighboring centroids Figure S13f. From this plot we found that the average separation of clumps is 45 ± 11 μm. Additionally we can extract the distribution for sizes of the spots. We found the the average radius of the clump is 14 μm.

6. Moran's I

Moran's I was developed to measure spatial autocorrelation and indicates whether adjacent observations of the same phenomenon are correlated. Moran's I was proposed as follows (26)

$$I = \frac{N}{\sum_{i=1}^{N}\sum_{j=1}^{N} w_{ij}} \frac{\sum_{i=1}^{N}\sum_{j=1}^{N} w_{ij}(x_i - \bar{x})(x_j - \bar{x})}{\sum_{i=1}^{N}(x_i - \bar{x})^2} \quad [40]$$

where N is the total number of pixels, x is the variable of interest (red fluorescence level here), $\bar{x}$ is the mean of x, and w_{ij} a weight matrix of pixels. We employ a simple form of the weight matrix as follows: $w_{ij} = 1$ if two pixels are directly adjacent and $w_{ij} = 0$ otherwise. Moran's I values typically range from $+1$, representing complete positive spatial autocorrelation, to -1, corresponding to complete negative spatial autocorrelation.

7. A deterministic reaction-diffusion model

The goal of this section is to see if a deterministic model can reproduce the principal features of the observed pattern. To this end, we use order of magnitude estimates for parameters. Our synthetic system consists of biochemical reactions involving promoters, mRNA, and proteins as well as signal diffusion, with rate constants that span multiple time-scales. To obtain a manageable model, we make the following commonly used simplifying assumptions:

- Operator states of a promoter fluctuate much faster than protein degradation rates.
- mRNA half-life is much shorter than protein half-life.

These assumptions allow us to eliminate operator fluctuation and mRNA kinetics and model the system at the communication signals and protein levels as

$$\frac{\partial U}{\partial t} = \alpha_u I_u - \gamma_u U + D_u \nabla^2 U \quad [41]$$

$$\frac{\partial V}{\partial t} = \alpha_v I_v - \gamma_v V + D_v \nabla^2 V \quad [42]$$

$$\frac{\partial I_u}{\partial t} = \alpha_{iu} F_1(X_1, C) - \gamma_{iu} I_u \quad [43]$$

$$\frac{\partial I_v}{\partial t} = \alpha_{iv} F_1(X_1, C) - \gamma_{iv} I_v \quad [44]$$

$$\frac{\partial C}{\partial t} = \alpha_c F_2(X_2, L) - \gamma_c C \quad [45]$$

where U and V are the concentrations of the two diffusible morphogens $A_{3OC12HSL}$ and I_{C4HSL}, I_u and I_v are the concentrations of corresponding AHL synthases, and C refers to CI.

We model the hybrid promoters using the following Hill functions:

$$F_1(X_1,C) = \frac{[1+f_1(\frac{X_1}{K_{d1}})^{\theta_1}][1+f_2^{-1}(\frac{C}{K_{d2}})^{\theta_2}]}{[1+(\frac{X_1}{K_{d1}})^{\theta_1}][1+(\frac{C}{K_{d2}})^{\theta_2}]} \quad [46]$$

$$F_2(X_2,L) = \frac{[1+f_3(\frac{X_2}{K_{d3}})^{\theta_3}][1+f_4^{-1}(\frac{L}{K_{d4}})^{\theta_4}]}{[1+(\frac{X_2}{K_{d3}})^{\theta_3}][1+(\frac{L}{K_{d4}})^{\theta_4}]} \quad [47]$$

where $F_1(X_1,C)$ and $F_2(X_2,L)$ are the production rates of the promoters $P_{Las-OR1}$and $P_{Rhl-lacO}$, X_1 and X_2 are the LasR-$A_{3OC12HSL}$ complex and the RhlR-I_{C4HSL} complex respectively, and L is the concentration of unbound LacI protein. We use the definitions

$$X_1 = R_u U \quad [48]$$

$$X_2 = \frac{R_v V}{(1+U/K_{c3})} \quad [49]$$

$$L = \lambda_l \left(\frac{1+f_6^{-1}(I/K_{d6})^{\theta_6}}{1+(I/K_{d6})^{\theta_6}} \right) \quad [50]$$

where I is the IPTG concentration, R_u and R_v are the regulatory proteins LasR and RhlR:

$$R_u = \lambda_u I_u \quad [51]$$

$$R_v = \lambda_v \left(\frac{1+f_5^{-1}(C/K_{d5})^{\theta_5}}{1+(C/K_{d5})^{\theta_5}} \right) \quad [52]$$

A summary of the variables used in our model is available in Table S5 and definitions of the rate constants in Tables S6-S7. Hill functions employed in this model have a shared form of $Y = \frac{1+f(X/K)^{\theta}}{1+(X/K)^{\theta}}$, where X and Y correspond to the input and output of the function, K is the dissociation constant, θ is the Hill coefficient and f is the fold change of Y upon full induction by X. For the measured values of $\frac{D_v}{D_u} \approx 21.6$, deterministic patterns do not arise. We artificially increased this ratio to 100 and found that patterns did form with similar attributes to the observed pattern, but also were more regular than the patterns observed in our experiment.

To study patterning using our model, we divide a cellular lawn into a mesoscopic $M \times M$ grid ($M = 64$ in our simulation). As is common for deterministic Turing simulations, we introduce small variation into the initial concentrations of the molecules for initial symmetry breaking. All the variables (species) were initially assigned low values (random values obeying a Gaussian distribution that has a mean of 1.0 and a variance of 0.05) to approximate the initial condition in our experimental setup. We numerically integrate the partial differential equations over time to simulate spontaneous pattern formation. We also perform numerical simulations with a range of IPTG concentrations (from 10^{-6} to 10^{-2} M) to explore modulation of pattern formation. Sizes of simulated patterns are determined in terms of relative fluorescence intensities rather than absolute values to match our image processing procedures for the experimental data.

8. A stochastic model

When the diffusion rate ratio is high enough to support pattern formation, our deterministic model correlates well with several characteristics of our experimental observations including pattern modulation by inducer IPTG. However, the deterministically simulated patterns have a uniform distribution of spot size, fluorescence intensity, and separation, whereas the experimental results display large variability in these attributes. We developed a stochastic spatiotemporal model to improve the correlation with the experimental observations. The patterning process is modeled with exactly the same biochemical reactions used in our deterministic model but simulated stochastically using an efficient tau-leaping stochastic algorithm(27, 28). To speed up this large scale spatiotemporal simulation, we employ a hybrid technique where all intracellular chemical reactions are stochastic but signal diffusion is deterministic since the diffusion time scales are typically much faster than the intracellular reactions considered in our model.

To illustrate the behavior of each species in our pattern formation system (Table S5), we performed a spatial stochastic simulation using the parameters depicted in Tables S6-S7. The top of Figure S16 shows $A_{3OC12HSL}$ and I_{C4HSL} patterns produced in our stochastic simulation using the parameters given in tables Tables S6-S7. The red line indicates the location of the cross-section used for all other

dynamic variables. The bottom of Figure S16 shows cross-sectional slices of variables U ($A_{3OC12HSL}$), V (I_{C4HSL}), I_u (LasI), I_v (RhlI), C (CI), R_u (LasR), R_v (RhlR), L (free LacI), X_1 (LasR-$A_{3OC12HSL}$ complex), and X_2 (RhlR-I_{C4HSL} complex).

As seen in Figure S16, the concentrations of LasI, RhlI, and LasR are proportional to the $A_{3OC12HSL}$ activator. This is due to the fact that these proteins are expressed from the $A_{3OC12HSL}$ activated $P_{Las-OR1}$ promoter. Likewise, the LasR-$A_{3OC12HSL}$ complex is directly proportional to $A_{3OC12HSL}$ concentrations. In addition, since RhlI catalyzes I_{C4HSL} synthesis, I_{C4HSL} is also directly proportional to $A_{3OC12HSL}$ concentrations. However, since I_{C4HSL} diffuses faster than $A_{3OC12HSL}$, relatively high concentrations of I_{C4HSL} are also found in between the $A_{3OC12HSL}$ activation domains.

Interestingly, the RhlR-I_{C4HSL} complex is inversely proportional to $A_{3OC12HSL}$. In regions of high $A_{3OC12HSL}$, $A_{3OC12HSL}$ competitively binds RhlR, lowering the concentration of the RhlR-I_{C4HSL} complex. However, as mentioned, I_{C4HSL} concentrations remain relatively high outside of the $A_{3OC12HSL}$ activation domains. Thus, RhlR-I_{C4HSL} is highest in between the activation domains. Collectively, this behavior results in green fluorescence (following the RhlR-I_{C4HSL} complex concentration) surrounding red fluorescent activation domains (following the LasR-$A_{3OC12HSL}$ complex concentration).

To characterize the stochastic simulation we calculated the distribution of spot sizes and spacing. We binarized the simulation data shown in Figure S17 and determined locations of the centroids of spots and the areas of the spots. The spacing is calculated by finding the distance to the nearest neighboring centroid. The distribution of spot sizes and spacing is shown in Figure S18. As the IPTG concentration is increased spot sizes decrease and have more variance. Similarly the spacing between spots decreases as the IPTG concentrations is increased.

To determine the sensitivity of the stochastic model to the parameters chosen, we individually varied parameters from half their nominal value to 1.5x their nominal value while keeping all other parameters fixed. For each set of parameters we calculate the analytical power spectrum and the eigenvalues of the Jacobian (linear stability matrix) of the stochastic model evaluated at a fixed point found numerically. We classify each set of parameters as either producing an unstable homogeneous state at wavenumber $k = 0$, a stable homogeneous state, a stochastic Turing pattern, or a deterministic Turing pattern. We classify a set of parameters as producing a pattern if they produce a peak in the calculated power spectrum at a nonzero wavenumber. To distinguish between stochastic Turing patterns and deterministic Turing patterns we examine the eigenvalues of the corresponding Jacobian. If the real part of all the eigenvalues is negative for all wavenumbers then the pattern must be due to stochasticity. If there is any range of wavenumbers that have corresponding positive real parts of their eigenvalues then the pattern is produced by the traditional Turing mechanism.

The results of this analysis are presented in Figure S22. This phase diagram indicates parameter ranges that produce unstable fixed points in red, stochastic patterns in blue, deterministic Turing pattern in green, and homogeneous stable states in magenta. To determine the sensitivity of the system to particular parameters we examined how the maximum eigenvalue of the Jacobian changed. In Figure S23 we have plotted the change in the real part of the maximum eigenvalue as a parameter is varied from half of its value to 1.5x its value. Positive changes, colored in red, indicate that increasing the corresponding parameter promotes traditional Turing patterns. Negative values, colored in blue, indicate that increasing the corresponding parameter promotes stochastic patterns. The amplitude of the change gives an indication of the sensitivity of the parameter.

We also used Latin hypercube sampling to randomly generate 500 parameter sets where all the parameters were allowed to vary between half their nominal value and 1.5x their nominal value. For this analysis we found that 24.8% of parameters produced unstable fixed points, 43.2% produced stable homogeneous states, 13.2% produced stochastic Turing patterns, and 18.8% produced Turing patterns. This shows that this complex stochastic model can produce the same behaviors as our effective model. Additionally it shows that by including stochasticity, the range in which patterns can form has been increased by 70%.

To calculate the analytic power spectrum we used a method similar to that described in S9. We wrote down the transition probabilities for the stochastic model directly from our deterministic model. For example, the transition probability for U gaining a particle is $T(U \to U+1) = \alpha_u I_u$ and the transition probability for U losing a particle is $T(U \to U-1) = \gamma_u U$. Using a system size expansion one can derive Langevin equations governing the fluctuations of the form

$$\partial_t x = Ax + \xi \text{ where } \left\langle \xi(t)\xi^{\dagger}(t') \right\rangle = B\delta(t-t'), \quad [53]$$

where in the case of this model

$$\begin{aligned} A &= J - \mathrm{diag}([D_u k^2, D_v k^2, 0, 0, 0]) && [54] \\ B &= \mathrm{diag}([\alpha_u I_u + \gamma_u U + D_u k^2 U, \alpha_v I_v + \gamma_v V + D_v k^2 V, \\ &\quad \alpha_{iu} F_1(X_1, C) + \gamma_{iu} I_u, \alpha_{iv} F_1(X_1, C) + \gamma_{iv} I_v, \\ &\quad \alpha_c F_2(X_2, L) + \gamma_c C]) && [55] \\ x^{\dagger} &= [\delta U, \delta V, \delta I_u, \delta I_v, \delta C], && [56] \end{aligned}$$

and J is the Jacobian of the model evaluated at the fixed point. Using these equations the power spectrum is calculated to be $P(k, w=0) = \langle xx^{\dagger} \rangle = A^{-1} B (A^{-1})^{\dagger}$. The fixed point, Jacobian, and power spectrum are numerically calculated using a custom Matlab script. Figure S24 shows the calculated power spectrum corresponding to the parameters listed in Table S6. In this figure the full model produces power spectrum with a power law tail of -2 for the inhibitor and an initial power law tail of -4 for the activator before undergoing a crossover to a -2 power law. The eigenvalues of the spatially extended Jacobian, A, are plotted in Figure S25 showing that all eigenvalues are negative. This indicates that the set of parameters in Table S6 produces a stochastic Turing pattern.

9. Stochastic Turing Patterns

In many biological and physical problems, noise is understood as a destabilizing agent. It thus comes as a surprise that when Turing-like systems are subject to noise, noise acts as a stabilizing agent for the spatially patterned state, enlarging its regime in the phase diagram. For both the case of noise external to the system (extrinsic noise) and noise associated with the discrete creation and annihilation of chemicals (demographic noise), patterns exist for a wider range of parameter space than would be the case deterministically(29, 30). The demographic noise of the signaling molecules, where one acts as an activator of gene expression and another an inhibitor, relax the criteria for separation of diffusion scales and enlarge the parameter space in which patterns should form. Patterns of this type are known as stochastic Turing patterns. Predictions for the power spectrum, the characteristic scale, and parameter regime in which stochastic Turing patterns form have been made by Butler and Goldenfeld (29).

A. Power spectra analysis of experimental observations. To test the predictions of stochastic Turing pattern theory we constructed power spectra for the experimental data. We converted the pictures of red and green fluorescent proteins into gray scale images and subtracted off the mean intensity to obtain data corresponding to the fluctuations. We then conducted a discrete two-dimensional (2D) Fourier transform of the data, finding its amplitude squared. Since it is clear from the resulting Fourier transforms that the patterns are isotropic, we perform an angular average (Figure S13a). The resulting radial power spectrum can be compared to the predictions made by Butler and Goldenfeld (29) (Figure S13c). By fitting the tail we find a power law with $\sigma = -2.3 \pm 0.4$ consistent with demographic noise. It is possible to obtain anomalous power law tails in the power spectrum due to discontinuities in the boundaries of the picture, but these artifacts are distinguishable by their lack of noise, and we are confident that such spectral leakage is not being observed in these data. The Fourier transform for the red fluorescent channel is not isotropic and the corresponding radial power spectrum has a power law with $\sigma = -3.9 \pm 0.4$ (Figure S13b,d). Radial power spectra were also calculated for other concentrations of IPTG as shown in figures S14 and S15. The spectra produced are also consistent with predictions of demographic noise.

B. Stochastic Turing pattern model. The traditional Turing mechanism usually consists of at least two chemicals. One of the chemicals is a slowly diffusing activator, activating the synthesis of itself and the inhibitor. The other chemical is a fast diffusing inhibitor, inhibiting synthesis of the activator and itself. The Turing mechanism can be explained by a simple qualitative argument consisting of three steps. Initially activator and inhibitor are distributed randomly. Areas with local concentrations of activator will autocatalytically

grow, forming dense clumps of activator. Inhibitor will also be produced near these clumps of activator. The rapidly diffusing inhibitor will suppress the spread of the clumps of activator. This simple picture of activator-inhibitor dynamics does not require large separation of diffusion rates or depend on details of rates. When this system is considered classically, however, it is found to either require fine tuning of reaction rates or have a large separation of diffusion rates. We will see shortly that the stochastic treatment solves this fine tuning problem.

Our synthetic system is system is designed to implement an activator-inhibitor system with $A_{3OC12HSL}$ as an activator of its own synthesis and that of I_{C4HSL}, while I_{C4HSL} is an inhibitor of both chemicals. To develop a simplified model of the activator inhibitor circuit, one can write down reaction diffusion equations for this system that are mathematically equivalent to the Levin-Segel model of herbivore-plankton interaction (31).

$$\partial_t \phi = \mu \nabla^2 \phi + b\phi + e\phi^2 - p\psi\phi \quad [57]$$

$$\partial_t \psi = \nu \nabla^2 \psi + p\psi\phi - d\psi^2 \quad [58]$$

Here ϕ is the concentration of activator ($A_{3OC12HSL}$), ψ is the concentration of inhibitor (I_{C4HSL}), μ and ν are the the diffusion constants of the activator and inhibitor respectively. The term $p\psi\phi$ is a competition term, $e\phi^2$ is a nonlinear activation term, and $-d\psi^2$ is a nonlinear self inhibition term for the inhibitor. These equations exhibit a Turing instability when (31):

$$\frac{\nu}{\mu} > \left(\frac{1}{\sqrt{p/d} - \sqrt{p/d - e/p}} \right)^2. \quad [59]$$

To consider the effects of extrinsic noise we can simply add white noise ξ to the system of equations above. Then we can construct the Fourier transformed stability matrix and solve for the power spectrum $\hat{P}(k,w)$ where k is the wave-number and w is frequency. When this is done it is found that the power spectrum has a power law tail, $\hat{P}(k, w=0) = \frac{k^\sigma}{\nu^2} \langle \xi\, \xi \rangle, k \gg k_m$ with an exponent $\sigma = -4$ (29). In addition, the condition for pattern formation becomes $\frac{\nu}{\mu} > \frac{p}{e}$.

Intrinsic noise, represented for example by copy number fluctuations arising from stochastic gene expression, can be studied by writing down an individual level model for the activator and inhibitor. The following set of chemical reactions describe the effective activator-inhibitor system that we engineered:

$$\begin{array}{lll} A \xrightarrow{b} AA & AI \xrightarrow{p_1/V} I & II \xrightarrow{d/V} I \\ AA \xrightarrow{e/V} AAA & AI \xrightarrow{p_2/V} II & \end{array} \quad [60]$$

Here A is the activator ($A_{3OC12HSL}$) and I is the inhibitor (I_{C4HSL}) and V is the well-mixed patch size setting the strength of the fluctuations. From these first order reactions one can derive a master equation governing the probability of having m molecules of I and n molecules of A at a given time:

$$\begin{aligned} \partial t P(m,n) =& b[(n-1)P(m,n-1) - nP(m,n)] + \frac{e}{V}[(n-1)(n-2)P(m,n-1) - n(n-1)P(m,n)] \\ &+ \frac{p_1}{V}[m(n+1)P(m,n+1) - mnP(m,n)] + \frac{p_2}{V}[(m-1)(n+1)P(m-1,n+1) - mnP(m,n)] \\ &+ \frac{d}{V}[(m+1)mP(m+1,n) - m(m-1)P(m,n)] \end{aligned} \quad [61]$$

To introduce spatial variations, the master equation can be conveniently represented as a path integral, from which mean-field equations and Langevin equations with multiplicative noise governing the fluctuations are obtained by van Kampen expansion (29). We calculate the power spectrum $\hat{P}(k,w)$ as a function of frequency w and wave-number k, obtaining a power spectrum tail ($k \gg k_m$): $\hat{P}(k, w=0) \approx \frac{\psi}{\nu} k^\sigma$ (inhibitor), $\hat{P}(k, w=0) \approx \frac{\phi}{\mu} k^\sigma$ (activator) with $\sigma = -2$. Patterns arise when

$$\frac{\nu}{\mu} > \left(\frac{p}{e}\right) \frac{5 + 7(de/p^2)}{4 + 5(de/p^2) + 3(de/p^2)^2}. \quad [62]$$

Additionally the wavelength, λ, or characteristic spacing of the pattern turns out to be the same as that for a classical Turing pattern (29) and is found to be

$$\lambda = 2\pi\sqrt{\frac{2}{\phi}\frac{\mu\nu}{e\nu - p\mu}}. \quad [63]$$

C. Stochastic model power spectra analysis. We now discuss the origin of the exponent discussed above, from the standpoint of two models that we have constructed to analyze the data. The first model is a coarse-grained phenomenological or minimal model for the morphogens. The second model is a detailed stochastic model, described in SI 8. We will see that there are two factors contributing to the -2 exponent in the inhibitor channel and the -4 exponent in the activator channel, in the context of intrinsic noise. Note that extrinsic noise, if present, would lead to an exponent of -4, but in both channels. The first explanation is that activator channel had a very sharp threshold for expressing the red fluorescence and the pictures were overexposed. This overexposure can suppress the small-scale correlations in the patterns. This idea is supported by taking data from simulations of demographic-noise induced patterns and performing image operations on the data to simulate this effect. We ran the simulated data through an image dilation morphological operator with a disk structural element 1px in radius. The resulting power spectra have power law tails with $\sigma = -4$, even though the original data were intrinsic noise-induced, having a power law tail with $\sigma = -2$. Thus, an asymptotic power-law tail of -2 in the power spectrum appears as an effective exponent of -4 in the presence of overexposure. This is further supported by looking at the spectra in figures S14 and S15. These images, taken at other IPTG concentrations, were not overexposed and their spectra have power law tails with exponents closer to -2.

The second explanation uses the detailed stochastic model described in SI 8. This model also predicts power-law tails with $\sigma = -2$ for both the activator and inhibitor, at asymptotically large values of k, because, when coarse-grained, the model should be well-described by the phenomenological model for the morphogens alone. But for the range of parameters that we estimate are consistent with the experimental data, the detailed model also predicts that for a wide range of intermediate wavenumbers, there is an effective power-law with $\sigma = -4$ for the activator, before undergoing a crossover to a power law with $\sigma = -2$ at high wave-numbers. Our interpretation is that the experiment is indeed well-described by the detailed model, and that we are observing the behavior before the crossover point in the power spectrum of the RFP channel. Overexposure does not cause any additional change to the effective -4 exponent.

The measured diffusion ratio of $\frac{\nu}{\mu} = 21.6$ is too small to produce classical Turing patterns. In fact to produce patterns qualitatively similar to the ones observed, the diffusion constants must be separated by a factor on the order of 100 in our non-stochastic simulation (See figure 3f). We can also plot the estimated range of parameters for our effective model and compare them to regimes where normal Turing patterns form and stochastic Turing patterns form (Figure S13e). We see from this plot that the estimated parameters fall mainly in the regime where stochastic patterns form, but not where normal Turing patterns can form. Any parameters above the blue surface will form classical Turing patterns. Any parameters above the green surface can form stochastic Turing patterns. The yellow oval representing our estimated range of effective parameters falls mainly below the blue surface but is above the green surface, indicating most of the parameters fall within the regime of stochastic patterns. We estimated the values and ranges of the ratios $\frac{\nu}{\mu}$, $\frac{e}{p}$, and $\frac{d}{p}$ which solely control pattern formation in the reduced model. In our analysis we used the the experimentally measured ratio of diffusion constants $\frac{\nu}{\mu} = 21.6 \pm 10$ and we estimated $\frac{e}{p} < 1$ by using the knowledge that for any pattern to form, either classical or stochastic, the homogeneous state must first be stable so $p > e$. Finally since the degradation rate is always smaller than the rate of production of our molecules we estimated $\frac{d}{p} < 1$. Even at our measured values of diffusion constants our stochastic simulation continued to produce patterns similar to the ones observed in our experiment and produced a power spectrum power law tail with $\sigma - 2.4$ consistent with our experiment.

1. Gierer A, Meinhardt H (1972) A theory of biological pattern formation. *Biol. Cybern.* 12(1):30–39.
2. Whiteley M, Lee K, Greenberg E (1999) Identification of genes controlled by quorum sensing in Pseudomonas aeruginosa.
3. Schuster M, Lostroh C, Ogi T, Greenberg E (2003) Identification, timing, and signal specificity of Pseudomonas aeruginosa quorum-controlled genes: a transcriptome analysis. *J. Bacteriol.* 185(7):2066.
4. Schuster M, Urbanowski M, Greenberg E (2004) Promoter specificity in Pseudomonas aeruginosa quorum sensing revealed by DNA binding of purified LasR. *Proc. Natl. Acad. Sci. U.S.A.* 101(45):15833–15839.
5. Stewart P (2003) Diffusion in Biofilms. *J. Bacteriol.* 185(5):1485–1491.
6. Karig D (2007) Ph.D. thesis (Princeton University, Princeton, NJ).
7. Huang JJ, Han JI, Zhang LH, Leadbetter JR (2003) Utilization of acyl-homoserine lactone quorum signals for growth by a soil pseudomonad and Pseudomonas aeruginosa PAO1. *Appl Environ Microbiol* 69(10):5941–9.
8. Stricker J, et al. (2008) A fast, robust and tunable synthetic gene oscillator. *Nature* 456(7221):516–519.
9. Schaefer AL, Val DL, Hanzelka BL, Cronan, J. E. J, Greenberg EP (1996) Generation of cell-to-cell signals in quorum sensing: acyl homoserine lactone synthase activity of a purified Vibrio fischeri LuxI protein. *Proc Natl Acad Sci U S A* 93(18):9505–9.
10. Goldbeter A, Koshland, D. E. J (1981) An amplified sensitivity arising from covalent modification in biological systems. *Proc Natl Acad Sci U S A* 78(11):6840–4.
11. Gunawardena J (2005) Multisite protein phosphorylation makes a good threshold but can be a poor switch. *Proc Natl Acad Sci U S A* 102(41):14617–22.
12. Brenner K, Karig D, Weiss R, Arnold F (2007) Engineered bidirectional communication mediates a consensus in a microbial biofilm consortium. *Proc. Natl. Acad. Sci. U.S.A.* 104(44):17300.
13. Basu S, Mehreja R, Thiberge S, Chen M, Weiss R (2004) Spatiotemporal control of gene expression with pulse-generating networks. *Proc. Natl. Acad. Sci. U.S.A.* 101(17):6355–6360.
14. Karig D, Weiss R (2005) Signal-amplifying genetic circuit enables in vivo observation of weak promoter activation in the Rhl quorum sensing system. *Biotechnol Bioeng* 89(6):709–18.
15. Yokobayashi Y, Weiss R, Arnold FH (2002) Directed evolution of a genetic circuit. *Proc Natl Acad Sci U S A* 99(26):16587–91.
16. Andersen JB, et al. (1998) New unstable variants of green fluorescent protein for studies of transient gene expression in bacteria. *Appl Environ Microbiol* 64(6):2240–6.
17. Weiss R, Basu S (2002) The device physics of cellular logic gates in *NSC-1: The First Workshop on NonSilicon Computing.* pp. 54–61.
18. Pearson J, Pesci E, Iglewski B (1997) Roles of Pseudomonas aeruginosa las and rhl quorum-sensing systems in control of elastase and rhamnolipid biosynthesis genes. *J. Bacteriol.* 179(18):5756–5767.
19. Weiss R (2001) Ph.D. thesis (Massachusetts Institute of Techonology, Cambridge, MA).
20. Gardner T, Cantor C, Collins J (2000) Construction of a genetic toggle switch in Escherichia coli. *Nature* 403(6767):339–342.
21. Weiss R, Knight T (2001) Engineered communications for microbial robotics. *Lect. Notes. Comput. Sc.* 2054:1–16.
22. Verhulst P (1838) 'Notice sur la loi que la population poursuit dans son accroissement. *Correspondance Mathe-matique et Physique* 10:113–121.
23. Chen C, Riadi L, Suh S, Ohman D, Ju L (2005) Degradation and synthesis kinetics of quorum-sensing autoinducer in Pseudomonas aeruginosa cultivation. *J. Biotechnol.* 117(1):1–10.
24. Pearson J, Van Delden C, Iglewski B (1999) Active efflux and diffusion are involved in transport of Pseudomonas aeruginosa cell-to-cell signals. *Journal of bacteriology* 181(4):1203–1210.
25. Pesci E, Pearson J, Seed P, Iglewski B (1997) Regulation of las and rhl quorum sensing in Pseudomonas aeruginosa. *J. Bacteriol.* 179(10):3127–3132.
26. Moran P (1950) Notes on continuous stochastic phenomena. *Biometrika* 37:17–33.
27. Cao Y, Gillespie D, Petzold L (2006) Efficient step size selection for the tau-leaping simulation method. *J. Chem. Phys.* 124:044109.
28. Rossinelli D, Bayati B, Koumoutsakos P (2008) Accelerated stochastic and hybrid methods for spatial simulations of reaction–diffusion systems. *Chem. Phys. Lett.* 451(1-3):136–140.
29. Butler T, Goldenfeld N (2011) Fluctuation-driven turing patterns. *Physical Review E* 84(1):011112.
30. Biancalani T, Fanelli D, Di Patti F (2010) Stochastic turing patterns in the brusselator model. *Physical Review E* 81(4):046215.
31. Levin SA (1976) Hypothesis for origin of planktonic patchiness. *Nature* 259:659.

Table S5. Variables used in the model.

Symbol	Molecule
U	$3OC_{12}HSL$
V	C_4HSL
I_u	LasI
I_v	RhlI
C	CI
R_u	LasR
R_v	RhlR
L	free LacI
X_1	LasR-$3OC_{12}HSL$ complex
X_2	RhlR-C_4HSL complex

Table S6. Definitions and values for the rate constants used in our mathematical model.

Parameter	Description	Value	Unit
α_u	$A_{3OC12HSL}$ production rate	3.0×10^1	hr^{-1}
γ_u	$A_{3OC12HSL}$ degradation rate	1.0	hr^{-1}
D_u	$A_{3OC12HSL}$ diffusion coefficient	5.0×10^{-1}	$grid^2/hr$
α_v	I_{C4HSL} production rate	3.0×10^1	hr^{-1}
γ_v	I_{C4HSL} degradation rate	1.0	hr^{-1}
D_v	I_{C4HSL} diffusion coefficient	10.8 or 50^*	$grid^2/hr$
α_{iu}	Basal production rate of LasI	1.0×10^1	molecules/hr
γ_{iu}	Degradation rate of LasI	1.0	hr^{-1}
α_{iv}	Basal production rate of RhlI	0.3	molecules/hr
γ_{iv}	Degradation rate of RhlI	1.0	hr^{-1}
α_c	Basal production rate of CI	1.0×10^1	molecules/hr
γ_c	CI degradation rate	1.0	hr^{-1}
λ_u	Ratio between LasR and LasI	1.0	$\diagup$
λ_v	Steady state level of RhlR by $\lambda_{P(R-O1)}$ w/o CI regulation	1.0×10^3	molecules
λ_l	Steady state level of LacI from p_{lacq} expression	1.5×10^2	molecules
K_{c3}	$A_{3OC12HSL}$-RhlR dissociation constant	1.5×10^2	molecules
I	IPTG concentration	$1.0 \times 10^{-6\sim-2}$	M

Table S7. Additional definitions and values for the rate constants used in our mathematical model.

Parameter	Description	Value	Unit
θ_1	Hill coeff. for LasR-$A_{3OC12HSL}$ complex activation of $P_{Las-OR1}$	1.0	⁄
K_{d1}	Disso. constant of LasR-$A_{3OC12HSL}$ complex with $P_{Las-OR1}$	1.0×10^3	molecules
f_1	Fold change for full induction of $P_{Las-OR1}$	1.0×10^3	⁄
θ_2	Hill coeff. for CI repression of $P_{Las-OR1}$	2.0	⁄
K_{d2}	Disso. constant of CI with $P_{Las-OR1}$	1.0×10^1	molecules
f_2	Fold change for full inhibition of $P_{Las-OR1}$	1.0×10^5	⁄
θ_3	Hill coeff. for RhlR-I_{C4HSL} complex activation of $P_{Las-OR1}$	1.0	⁄
K_{d3}	Disso. constant of RhlR-I_{C4HSL} complex with pRhl-lacO	1.0×10^5	molecules
f_3	Fold change for full induction of pRhl-lacO	1.0×10^3	⁄
θ_4	Hill coeff. for the LacI activation of pRhl-lacO	4.0	⁄
K_{d4}	Disso. constant of LacI with pRhl-lacO	1.0×10^2	molecules
f_4	Fold change for full inhibition of pRhl-lacO	1.0×10^3	⁄
θ_5	Hill coeff. for the CI activation of $\lambda_{P(R-O1)}$	2.0	⁄
K_{d5}	Disso. constant of CI with $\lambda_{P(R-O1)}$	1.0×10^3	molecules
f_5	Fold change for full induction of $\lambda_{P(R-O1)}$	1.0×10^5	⁄
θ_6	Hill coeff. for the IPTG binding to LacI	1.0	⁄
K_{d6}	Disso. constant of IPTG with LacI	1.0×10^{-3}	M
f_6	Fold change of LacI activity for IPTG full induction	1.0×10^5	⁄

Figure Captions

Figure S1: Design of Turing pattern formation system. **a**, $A_{3OC12HSL}$ serves as the activator species and catalyzes its own synthesis as well as that of I_{C4HSL}. I_{C4HSL} is the inhibitor, as this signal ultimately represses production of $A_{3OC12HSL}$ and I_{C4HSL}. **b**, Initial genetic network implementation. $A_{3OC12HSL}$ binds LasR and activates p(Las)-OR1 promoters that express LasI and RhlI. LasI catalyzes synthesis of $A_{3OC12HSL}$, and RhlI catalyzes synthesis of I_{C4HSL}. I_{C4HSL} binds RhlR and activates p(Rhl)-OR1, which expresses CI, and CI represses the p(Las)-OR1 promoters in addition to p(Rhl)-OR1. **c**, Modeling results suggested that a design with a CI OR1 binding site in the promoter expressing RhlR instead of in p(Rhl) was more enriched for Turing instabilities. **d**, Placing LasR under control of the p(Las)-OR1 promoter effectively increases the p(Las)-OR1 response sensitivity to $A_{3OC12HSL}$. For clarity, arrows were not shown in (c) and (d) to indicate LasR binding $A_{3OC12HSL}$ and activating p(Las)-OR1 or RhlR binding I_{C4HSL} and activating p(Rhl).

Figure S2: Computational exploration of design variations. **a**, Several different designs were simulated with CI OR1 binding domains in different combinations of promoters and both with and without $A_{3OC12HSL}$ degrading acylase. In the simulations, a promoter contains an OR1 domain if the corresponding bit in the binary representation of the network number is a 1. Likewise, acylase is expressed only if bit_6 of the binary representation of the network number is 1. For example, $56_{10} = 0111000_2$, so Network 56 has an OR1 site in the p(Las)-OR1 promoters expressing LasI and RhlI and in the promoter expressing RhlR since bit_3, bit_4, and bit_5 are all 1. **b**, Number of random parameter sets found for each network. Although Network 106 was most enriched for Turing instabilities, this network requires acylase expression. Networks 56 and 57, depicted in Figure S1c, which do not require acylase expression were ultimately chosen instead.

Figure S3: Constitutive LasR and p(Las) controlled LasR. **a**, Genetic network with constitutively expressed LasR and a p(Las) promoter expressing a reporter gene. **b**, Genetic network with p(Las) expressing both a reporter and LasR. **c**, Reporter expression versus $A_{3OC12HSL}$ for these networks using the following parameters: $\alpha_0 = 0.01$, $\alpha_1 = 1$, $K = 0.5$, $d = 1$, $m = 1$.

Figure S4: Plasmids used in our patterning and control experiments. **a**, Plasmid pFNK-512 implements activation of $A_{3OC12HSL}$ and I_{C4HSL}. It corresponds to the upper part of the circuit diagram in Figure 1b in the main text. **b**, Plasmid pFNK-804-LacO-LacI corresponds the lower part of the circuit diagram. It implements inhibition of both signals. **c**, Plasmid pFNK806 is derived from pFNK804-LacO-LacI and provides better contrast between green and red fluorescence intensities. **d**, Plasmid pTOG-1 is a two-color bistable toggle switch. It is used to explore the role of collective commitment in pattern formation. **e-f**, pINV-5 and pASK-201 are IPTG-inducible plasmids that produce GFP and RFP correspondingly. Both are used in our control experiments. **g**, Sequences for the hybrid promoters $P_{Las-OR1}$ and $P_{Rhl-lacO}$.

Figure S5: Liquid AHL dosage response curves for the reporter cells. The red curve is the $A_{3OC12HSL}$ response of cells harboring pFNK-503-qscrsaL, a $A_{3OC12HSL}$ detector plasmid. The blue curve is the I_{C4HSL} response of cells harboring the receiver plasmid pFNK-202-qsc119, a I_{C4HSL} detector plasmid.

Figure S6: Comparison of our experimental data with modeling results. **a-b**, Fluorescence intensity of receiver cells in response to AHL gradients in 2% M9 agar plates. In both panels, the four curves correspond to hours 0, 2.5, 5, and 8.75. **c-d**, For simulations, fluorescence intensity simulation results were obtained using our mathematical model. The estimated diffusion coefficient for $A_{3OC12HSL}$ is 83 $\mu m^2/s$ and for I_{C4HSL} is 1810 $\mu m^2/s$.

Figure S7: Additional experiments to verify that diffusion rate calculations are reasonably robust to changing biofilm characteristcs over time. Fluorescence intensity of receiver cells in response to AHL gradients in 2% M9 agar plates.The four curves correspond to hours 0, 2.5, 5, and 8.

Figure S8: Competitive binding of $A_{3OC12HSL}$ to RhlR inhibits activation of promoter p_{Rhl} by I_{C4HSL}. **a**, GFP expression from p_{Rhl} promoter is induced by I_{C4HSL} (blue bar) but is not induced by $A_{3OC12HSL}$ (red bar). **b**, GFP expression from p_{Rhl} promoter decreases with $A_{3OC12HSL}$ for a fixed concentration of I_{C4HSL}.

Figure S9: Populations of *E. coli* expressing constitutive fluorescent reporter proteins GFP or mCherry were mixed in various ratios of

[Green:Red] on M9 supplemented minimal media and then imaged by microscopy. Scale bar, 200 µm.

Figure S10: Behavior of cell populations with each cell harboring an intracellular green/red bistable toggle switch. **a**, A bistable toggle switch derived from Gardner *et al* (20). **b**, Flow cytometry fluorescence density plot of the toggle cells at time 0. **c**, Flow cytometry fluorescence density plot of cells scraped from the cell lawn at 24 hours. **d**-**e**, Microscope images of cell lawns harboring the toggle switch circuit at 24 hours. Both RFP (**d**) and GFP (**e**) are homogeneously distributed and qualitatively different from that of a population carrying the emergent circuit in Fig. 2**a**. Scale bar, 100 µm. **f**, Fluorescence density plot of the microscope images in panels **d**-**e**.

Figure S11: Moran's I of the patterns from our deterministic simulations.

Figure S12: Emergence of patterns over time. Snapshots of red fluorescence were taken every 30 minutes for 32 hours. Shown are images in 4-hour intervals. Scale bar, 100 µm. Left: Average minimium distance between spots as a function of time, blue shading indicates standard deviation. Right: Average spot diameter as a function of time.

Figure S13: **a**, GFP image and corresponding Fourier transform. **c**, Radial power spectrum of GFP and power law fit of -2.3. **b**, RFP image and corresponding Fourier transform. **d**, Radial Power spectrum of RFP with a powerlaw tail fit of -3.9. **e**, Pattern forming regimes in parameter space and estimated parameters for our system. The parameters fall above the region where stochastic patterns form but below the region where normal Turing patterns form. **f**, Characteristic separation of spots with average separation of $32 \pm 8 px$ (45 ± 11 μm).

Figure S14: RFP images and their corresponding Radial Power spectrums with powerlaw tail fits of -2.5, -2.5, -2.9 for IPTG concentrations of 10^{-3} M, $10^{-2.5}$ M, and 10^{-2} M respectively.

Figure S15: GFP images and corresponding Radial Power spectrums with a powerlaw tail fits of -2.1, -2.2, -2.2 for IPTG concentrations of 10^{-3} M, $10^{-2.5}$ M, and 10^{-2} M respectively. At IPTG concentrations smaller than 10^{-4} M The green channel begins to look spatially homogeneous as the signal is not strong enough to show-up beyond the background camera noise.

Figure S16: $A_{3OC12HSL}$ and I_{C4HSL} patterns produced in our stochastic simulation using the parameters given in Tables S6-S7. The red line indicates the location of the cross-section used for all other dynamic variables. Cross-sectional slices of variables U ($A_{3OC12HSL}$), V (IC4HSL), I_u (LasI), I_v (RhlI), C (CI), R_u (LasR), R_v (RhlR), L (free LacI), X_1 (LasR-$A_{3OC12HSL}$ complex), and X_2 (RhlR-I_{C4HSL} complex).

Figure S17: $A_{3OC12HSL}$ patterns produced in our stochastic simulation using $D_v/D_u = 100$ and the parameters given in Tables S6-S7 for three different concentrations of IPTG.

Figure S18: Spot size and spacing distributions for 30C12HSL produced in our stochastic simulation with $D_v/D_u = 100$ for three different values of IPTG.

Figure S19: $A_{3OC12HSL}$ patterns produced in our stochastic simulation using the measured diffusion ratio of $D_v/D_u = 21.6$ and the parameters given in Tables S6-S7 for three different concentrations of IPTG.

Figure S20: 2D power spectrum and radial power spectrum for 30C12HSL produced in our stochastic simulation using $D_v/D_u = 21.6$ for three different values of IPTG.

Figure S21: Spot size and spacing distributions for 30C12HSL produced in our stochastic simulation using $D_v/D_u = 21.6$ for three different values of IPTG.

Figure S22: Phase Diagram showing the type of phase as each parameter is varied from half of its nominal value to 1.5x its nominal value while keeping all other parameters fixed. Red indicates an unstable fixed point, magenta a stable homogeneous state, blue a stochastic pattern, and green deterministic Turing pattern.

Figure S23: Sensitivity of a phase to a parameter is indicated by plotting the difference in eigenvalues between 1.5x the nominal value of a parameter and half of the nominal value. Red indicates a parameter that when increased promotes traditional Turing patterns and blue indicates a parameter promoting stochastic patterns.

Figure S24: The Analytic power spectrum calculated for the parameter set given in Tables S1-S2.

Figure S25: The real part of the eigenvalues of the Jacobian for the parameter set given in Tables S1-S2 plotted as a funtion of k. All the eigenvalues are negative indicating that the pattern formed is stochastic.

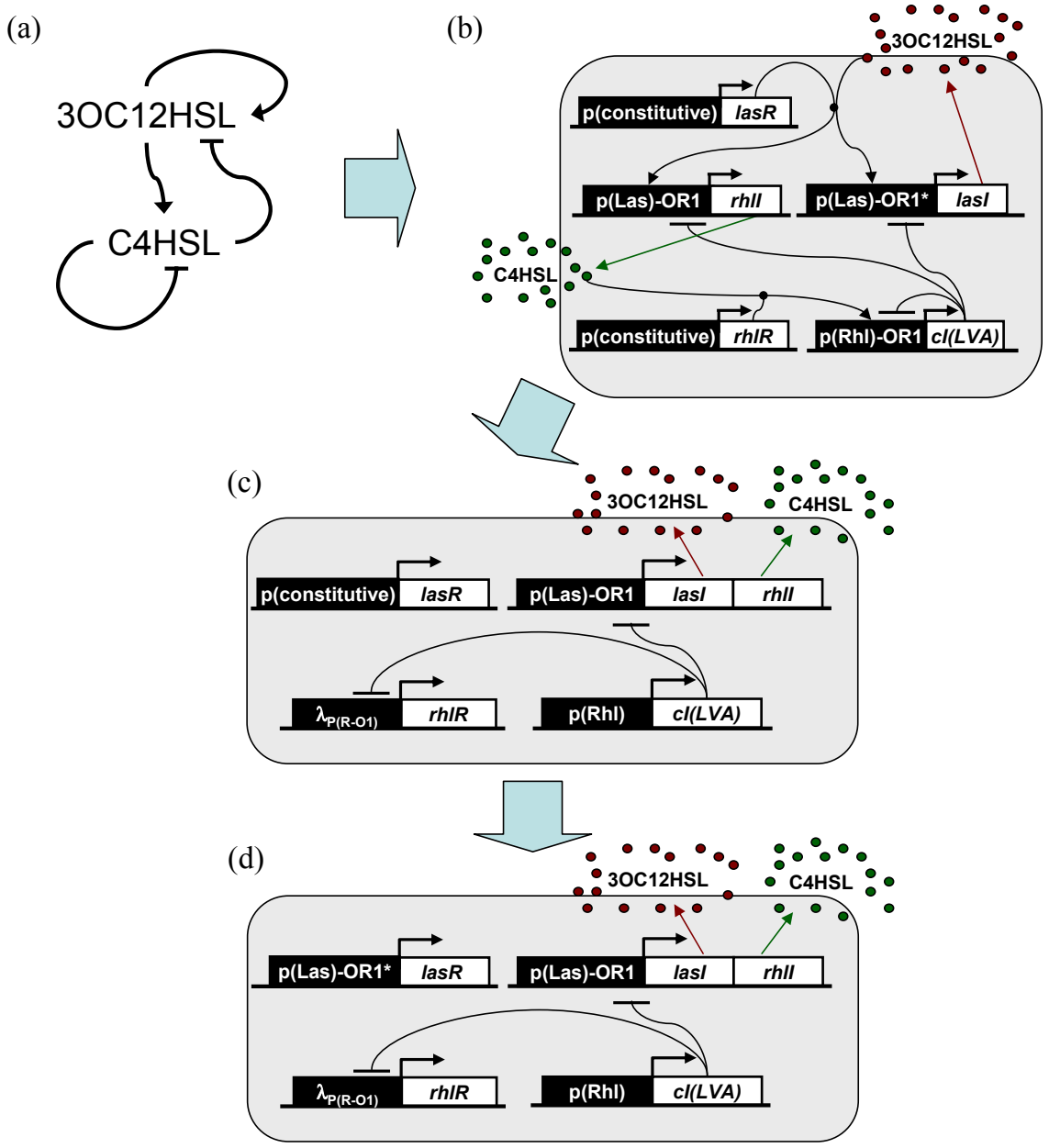

Fig. S1. Design of Turing pattern formation system. **a**, $A_{3OC12HSL}$ serves as the activator species and catalyzes its own synthesis as well as that of I_{C4HSL}. I_{C4HSL} is the inhibitor, as this signal ultimately represses production of $A_{3OC12HSL}$ and I_{C4HSL}. **b**, Initial genetic network implementation. $A_{3OC12HSL}$ binds LasR and activates p(Las)-OR1 promoters that express LasI and RhlI. LasI catalyzes synthesis of $A_{3OC12HSL}$, and RhlI catalyzes synthesis of I_{C4HSL}. I_{C4HSL} binds RhlR and activates p(Rhl)-OR1, which expresses CI, and CI represses the p(Las)-OR1 promoters in addition to p(Rhl)-OR1. **c**, Modeling results suggested that a design with a CI OR1 binding site in the promoter expressing RhlR instead of in p(Rhl) was more enriched for Turing instabilities. **d**, Placing LasR under control of the p(Las)-OR1 promoter effectively increases the p(Las)-OR1 response sensitivity to $A_{3OC12HSL}$. For clarity, arrows were not shown in (c) and (d) to indicate LasR binding $A_{3OC12HSL}$ and activating p(Las)-OR1 or RhlR binding I_{C4HSL} and activating p(Rhl).

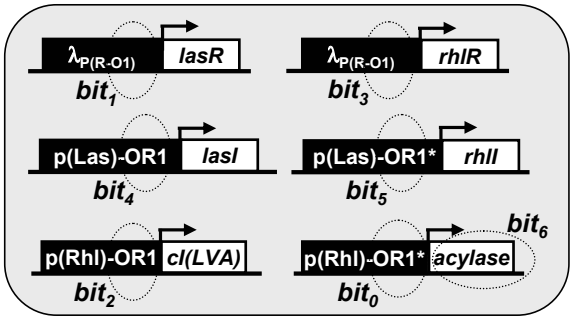

(a)

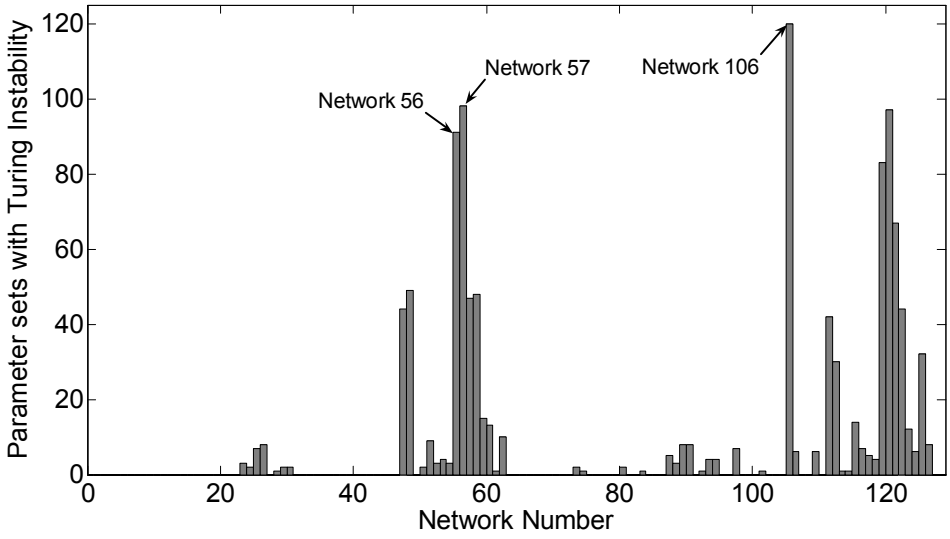

(b)

Fig. S2. Computational exploration of design variations. **a**, Several different designs were simulated with CI OR1 binding domains in different combinations of promoters and both with and without $A_{3OC12HSL}$ degrading acylase. In the simulations, a promoter contains an OR1 domain if the corresponding bit in the binary representation of the network number is a 1. Likewise, acylase is expressed only if bit_6 of the binary representation of the network number is 1. For example, $56_{10} = 0111000_2$, so Network 56 has an OR1 site in the p(Las)-OR1 promoters expressing LasI and RhlI and in the promoter expressing RhlR since bit_3, bit_4, and bit_5 are all 1. **b**, Number of random parameter sets found for each network. Although Network 106 was most enriched for Turing instabilities, this network requires acylase expression. Networks 56 and 57, depicted in Figure S1c, which do not require acylase expression were ultimately chosen instead.

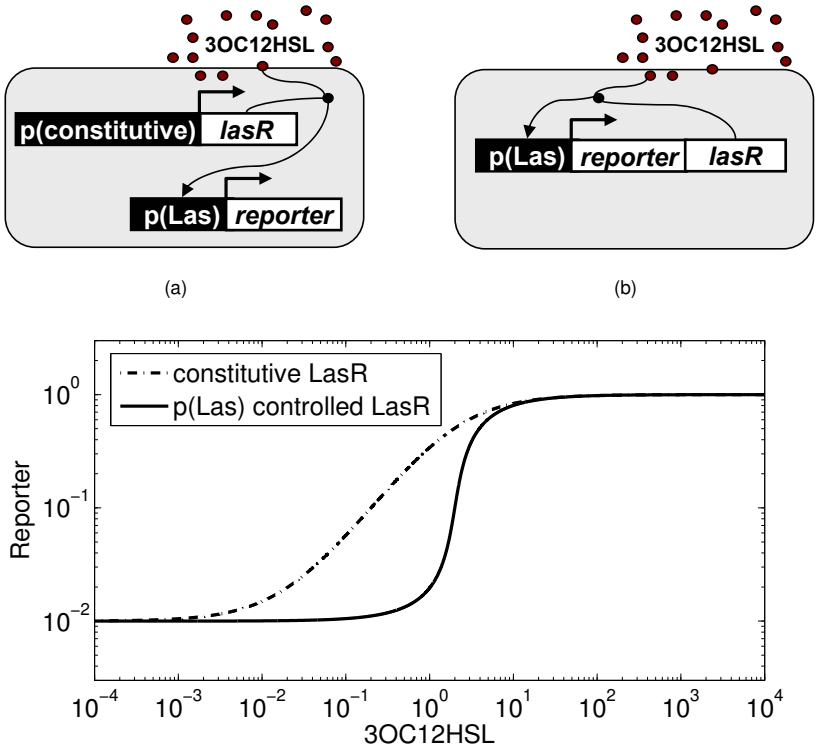

Fig. S3. Constitutive LasR and p(Las) controlled LasR. **a**, Genetic network with constitutively expressed LasR and a p(Las) promoter expressing a reporter gene. **b**, Genetic network with p(Las) expressing both a reporter and LasR. **c**, Reporter expression versus $A_{3OC12HSL}$ for these networks using the following parameters: $\alpha_0 = 0.01$, $\alpha_1 = 1$, $K = 0.5$, $d = 1$, $m = 1$.

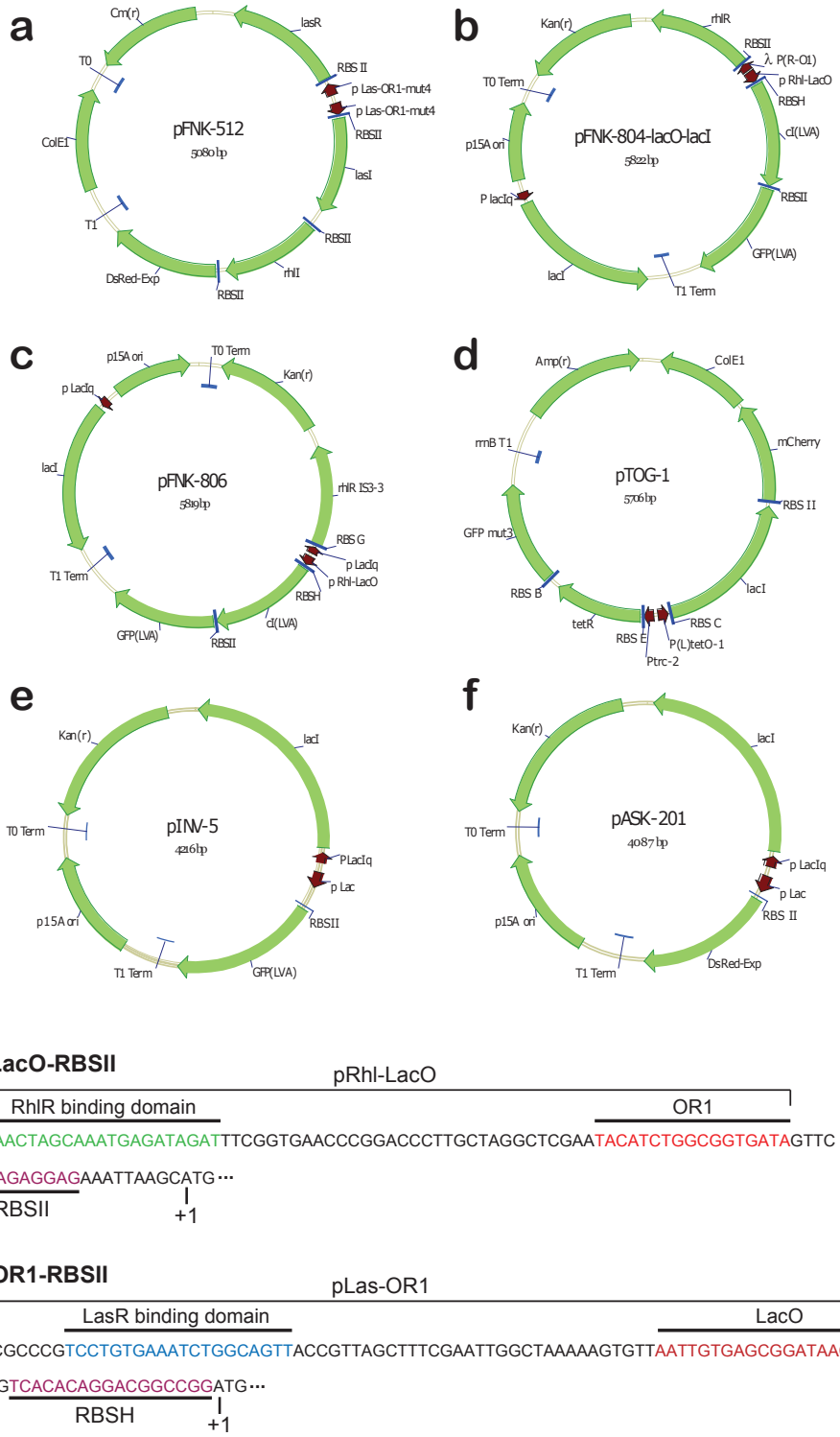

Fig. S4. Plasmids used in our patterning and control experiments. **a**, Plasmid pFNK-512 implements activation of $A_{3OC12HSL}$ and I_{C4HSL}. It corresponds to the upper part of the circuit diagram in Figure 1b in the main text. **b**, Plasmid pFNK-804-LacO-LacI corresponds the lower part of the circuit diagram. It implements inhibition of both signals. **c**, Plasmid pFNK806 is derived from pFNK804-LacO-LacI and provides better contrast between green and red fluorescence intensities. **d**, Plasmid pTOG-1 is a two-color bistable toggle switch. It is used to explore the role of collective commitment in pattern formation. **e-f**, pINV-5 and pASK-201 are IPTG-inducible plasmids that produce GFP and RFP correspondingly. Both are used in our control experiments. **g**, Sequences for the hybrid promoters $P_{Las-OR1}$ and $P_{Rhl-lacO}$.

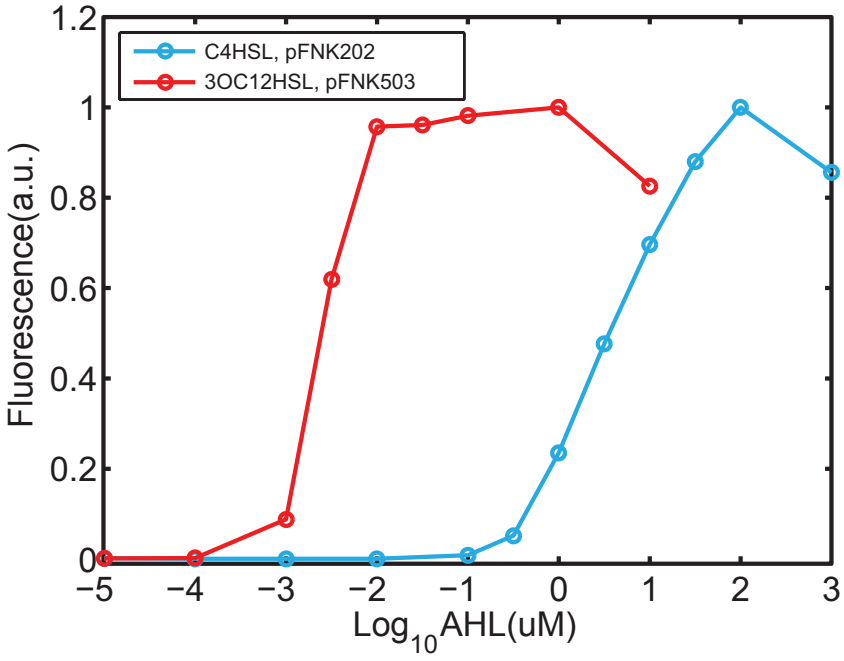

Fig. S5. Liquid AHL dosage response curves for the reporter cells. The red curve is the $A_{3OC12HSL}$ response of cells harboring pFNK-503-qscrsaL, a $A_{3OC12HSL}$ detector plasmid. The blue curve is the I_{C4HSL} response of cells harboring the receiver plasmid pFNK-202-qsc119, a I_{C4HSL} detector plasmid.

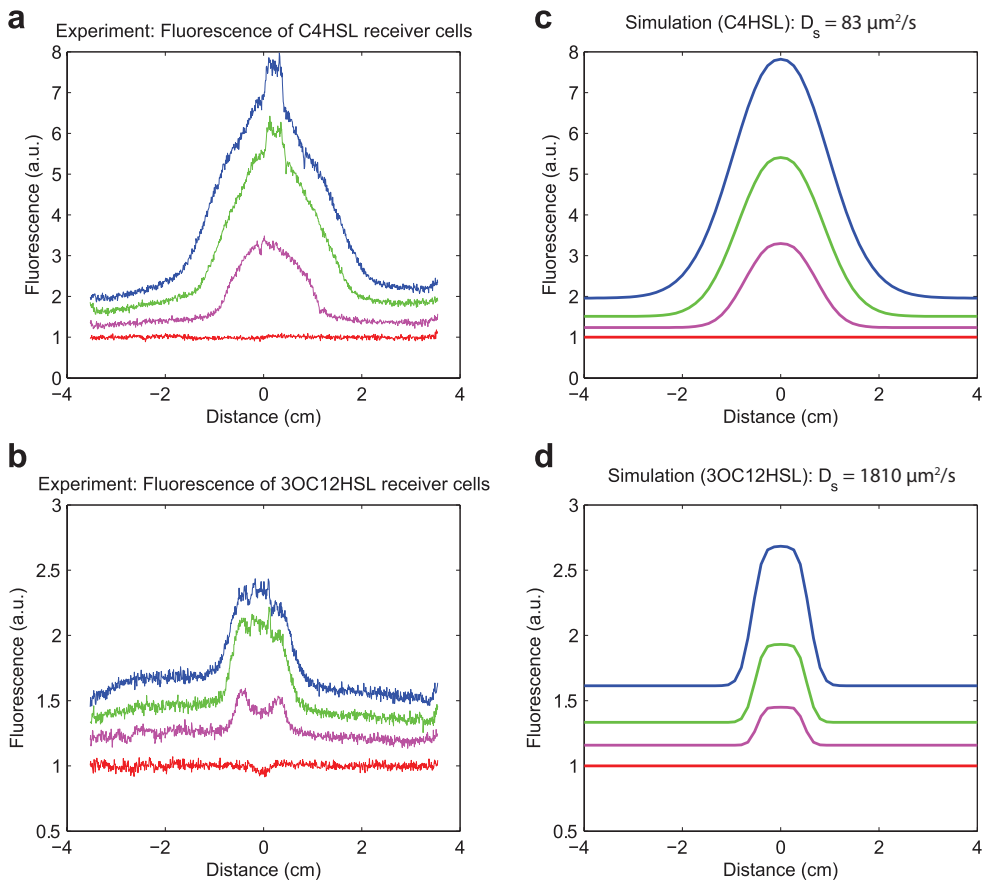

Fig. S6. Comparison of our experimental data with modeling results. **a-b**, Fluorescence intensity of receiver cells in response to AHL gradients in 2% M9 agar plates. In both panels, the four curves correspond to hours 0, 2.5, 5, and 8.75. **c-d**, For simulations, fluorescence intensity simulation results were obtained using our mathematical model. The estimated diffusion coefficient for $A_{3OC12HSL}$ is $83\,\mu m^2/s$ and for I_{C4HSL} is $1810\,\mu m^2/s$.

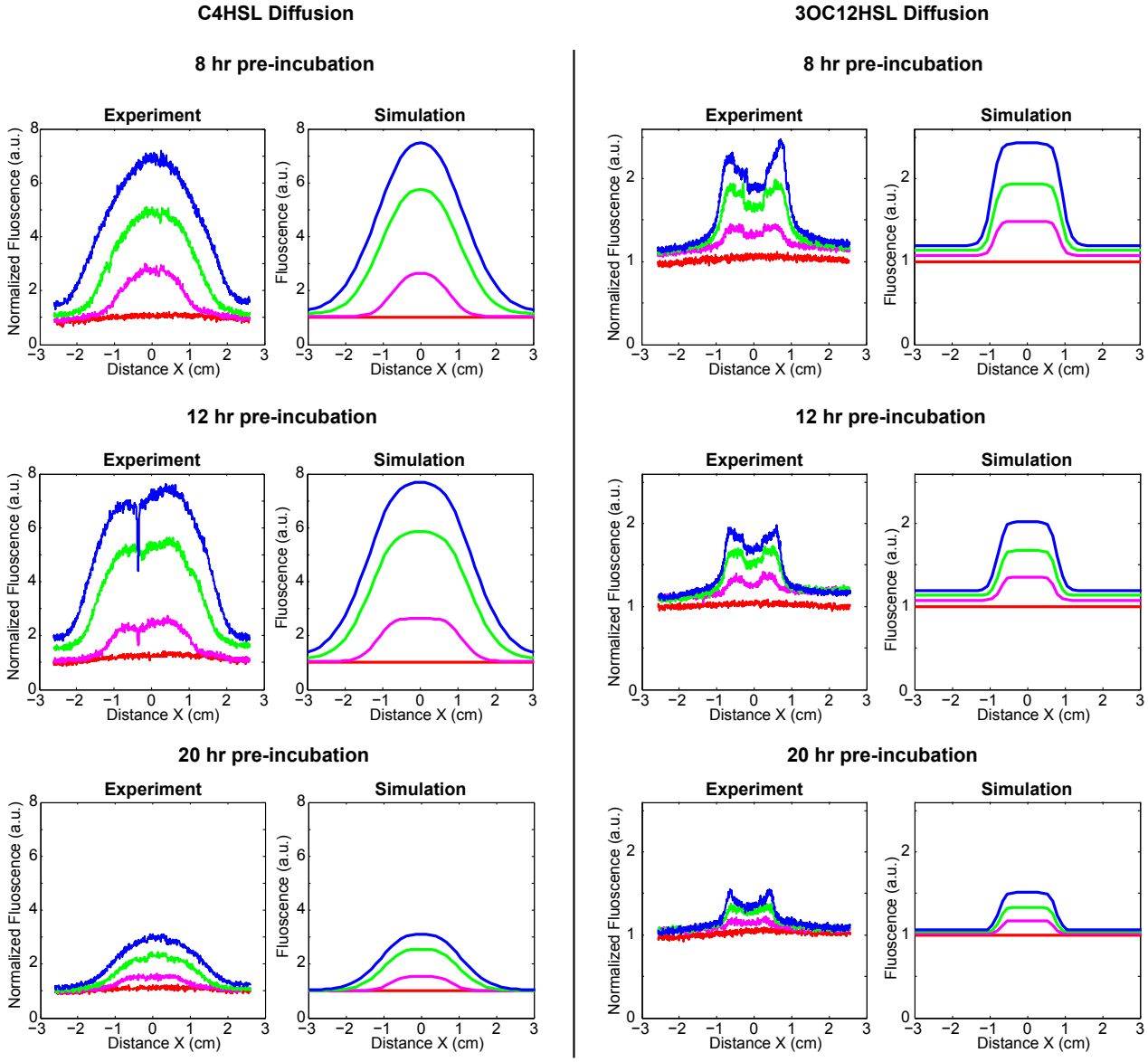

Fig. S7. Additional experiments to verify that diffusion rate calculations are reasonably robust to changing biofilm characteristcs over time. Fluorescence intensity of receiver cells in response to AHL gradients in 2% M9 agar plates.The four curves correspond to hours 0, 2.5, 5, and 8.

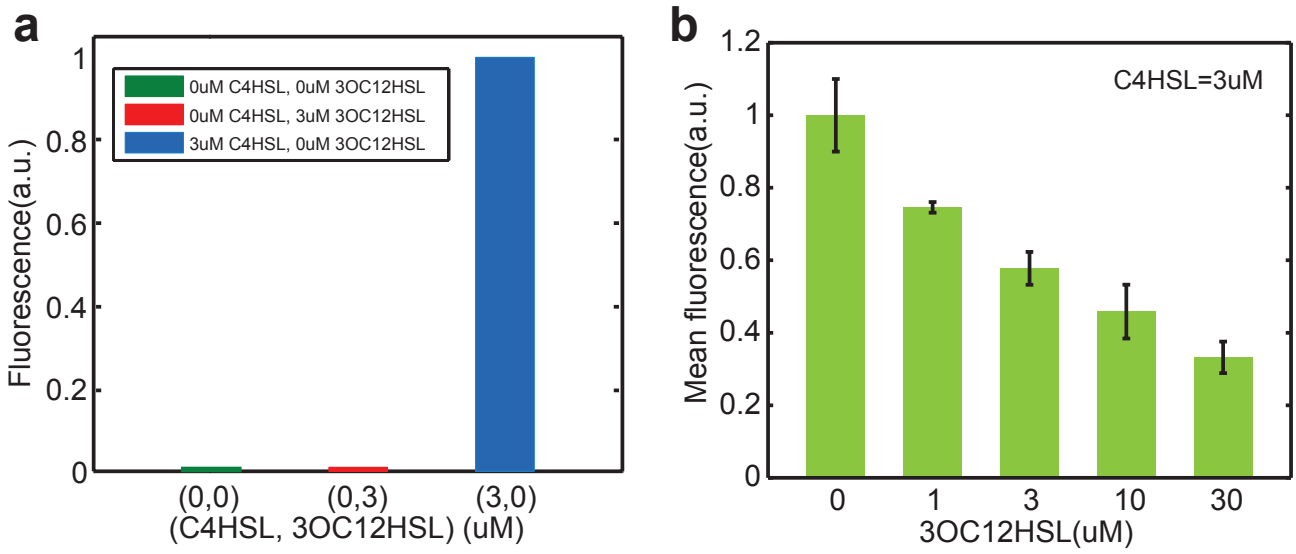

Fig. S8. Competitive binding of $A_{3OC12HSL}$ to RhlR inhibits activation of promoter p_{Rhl} by I_{C4HSL}. **a**, GFP expression from p_{Rhl} promoter is induced by I_{C4HSL} (blue bar) but is not induced by $A_{3OC12HSL}$ (red bar). **b**, GFP expression from p_{Rhl} promoter decreases with $A_{3OC12HSL}$ for a fixed concentration of I_{C4HSL}.

Fig. S9. Populations of *E. coli* expressing constitutive fluorescent reporter proteins GFP or mCherry were mixed in various ratios of [Green:Red] on M9 supplemented minimal media and then imaged by microscopy. Scale bar, $200\,\mu\mathrm{m}$.

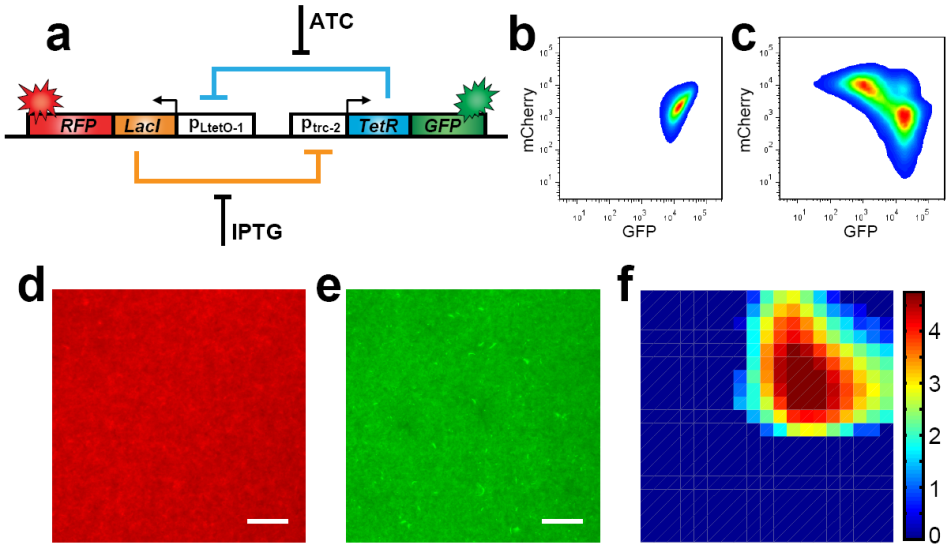

Fig. S10. Behavior of cell populations with each cell harboring an intracellular green/red bistable toggle switch. **a**, A bistable toggle switch derived from Gardner *et al* (20). **b**, Flow cytometry fluorescence density plot of the toggle cells at time 0. **c**, Flow cytometry fluorescence density plot of cells scraped from the cell lawn at 24 hours. **d**-**e**, Microscope images of cell lawns harboring the toggle switch circuit at 24 hours. Both RFP (**d**) and GFP (**e**) are homogeneously distributed and qualitatively different from that of a population carrying the emergent circuit in Fig. 2**a**. Scale bar, $100\,\mu\mathrm{m}$. **f**, Fluorescence density plot of the microscope images in panels **d**-**e**.

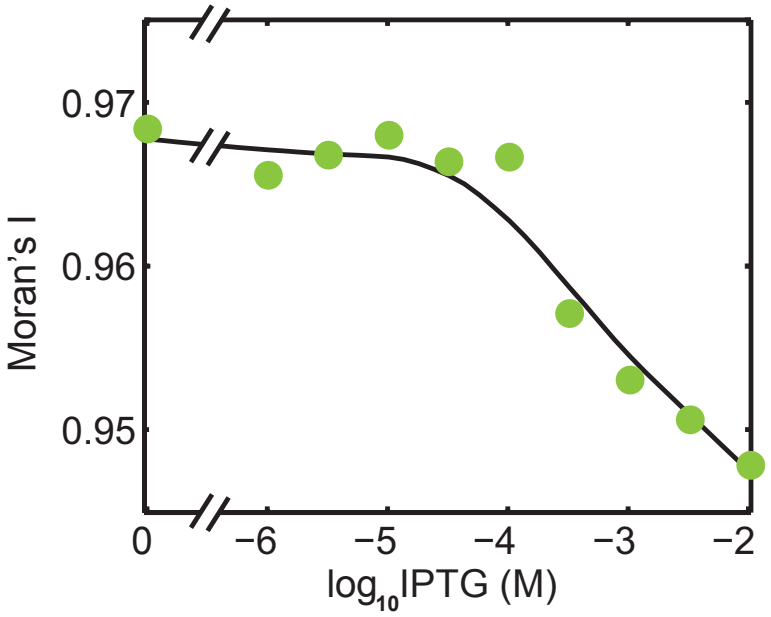

Fig. S11. Moran's I of the patterns from our deterministic simulations.

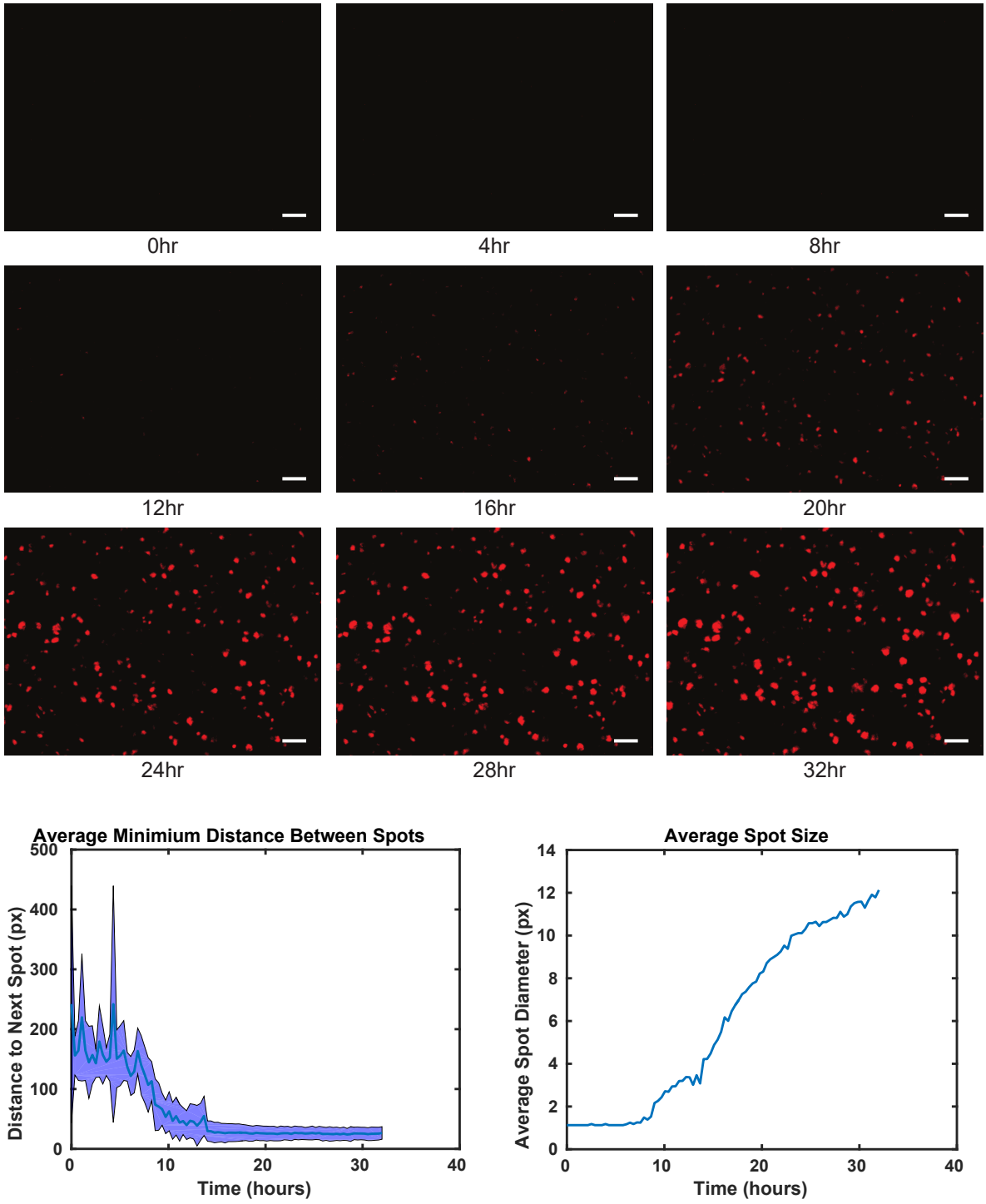

Fig. S12. Emergence of patterns over time. Snapshots of red fluorescence were taken every 30 minutes for 32 hours. Shown are images in 4-hour intervals. Scale bar, $100\,\mu\mathrm{m}$. Left: Average minimium distance between spots as a function of time, blue shading indicates standard deviation. Right: Average spot diameter as a function of time.

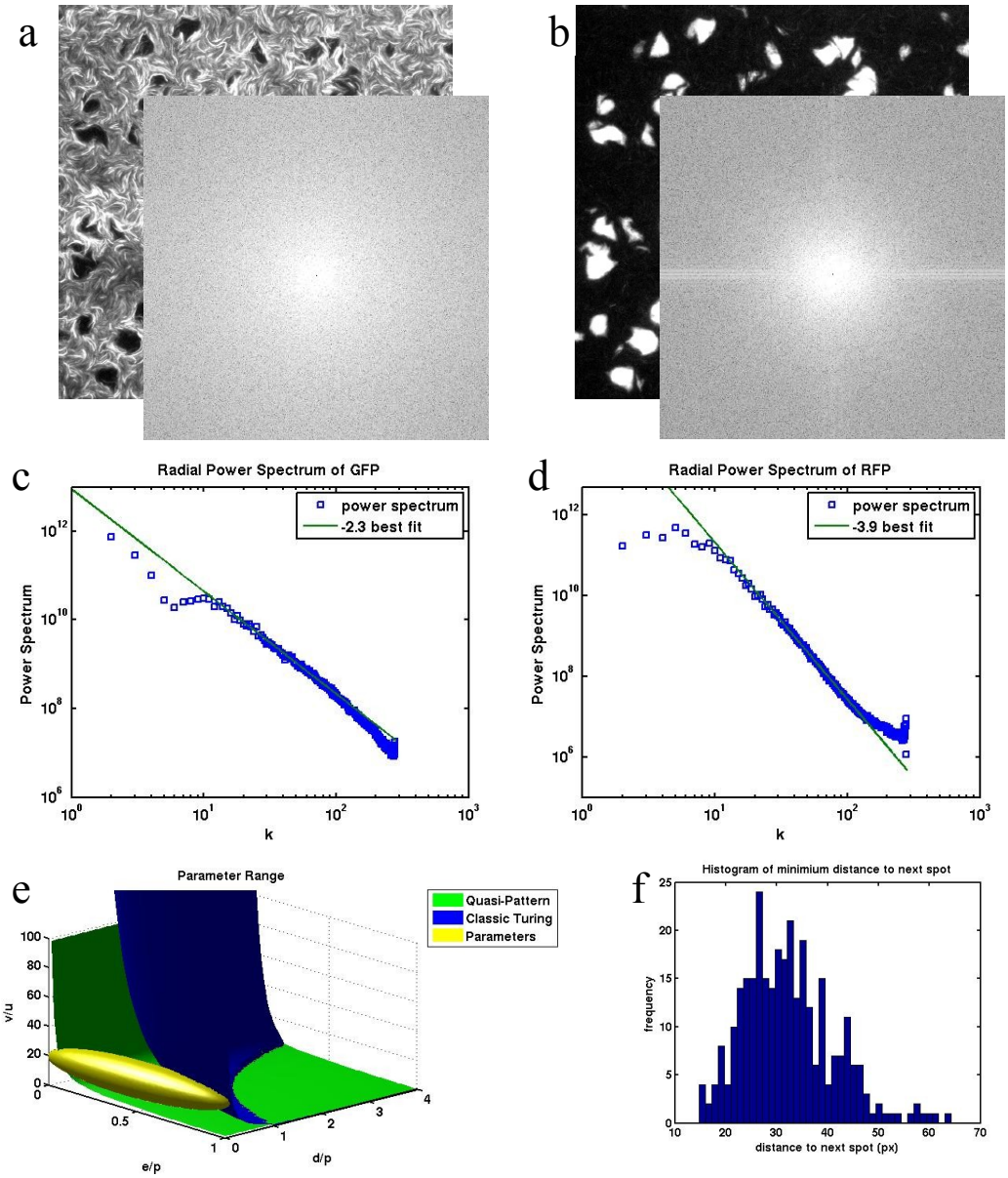

Fig. S13. a, GFP image and corresponding Fourier transform. **c**, Radial power spectrum of GFP and power law fit of -2.3. **b**, RFP image and corresponding Fourier transform. **d**, Radial Power spectrum of RFP with a powerlaw tail fit of -3.9. **e**, Pattern forming regimes in parameter space and estimated parameters for our system. The parameters fall above the region where stochastic patterns form but below the region where normal Turing patterns form. **f**, Characteristic separation of spots with average separation of $32 \pm 8px$ (45 ± 11 μm).

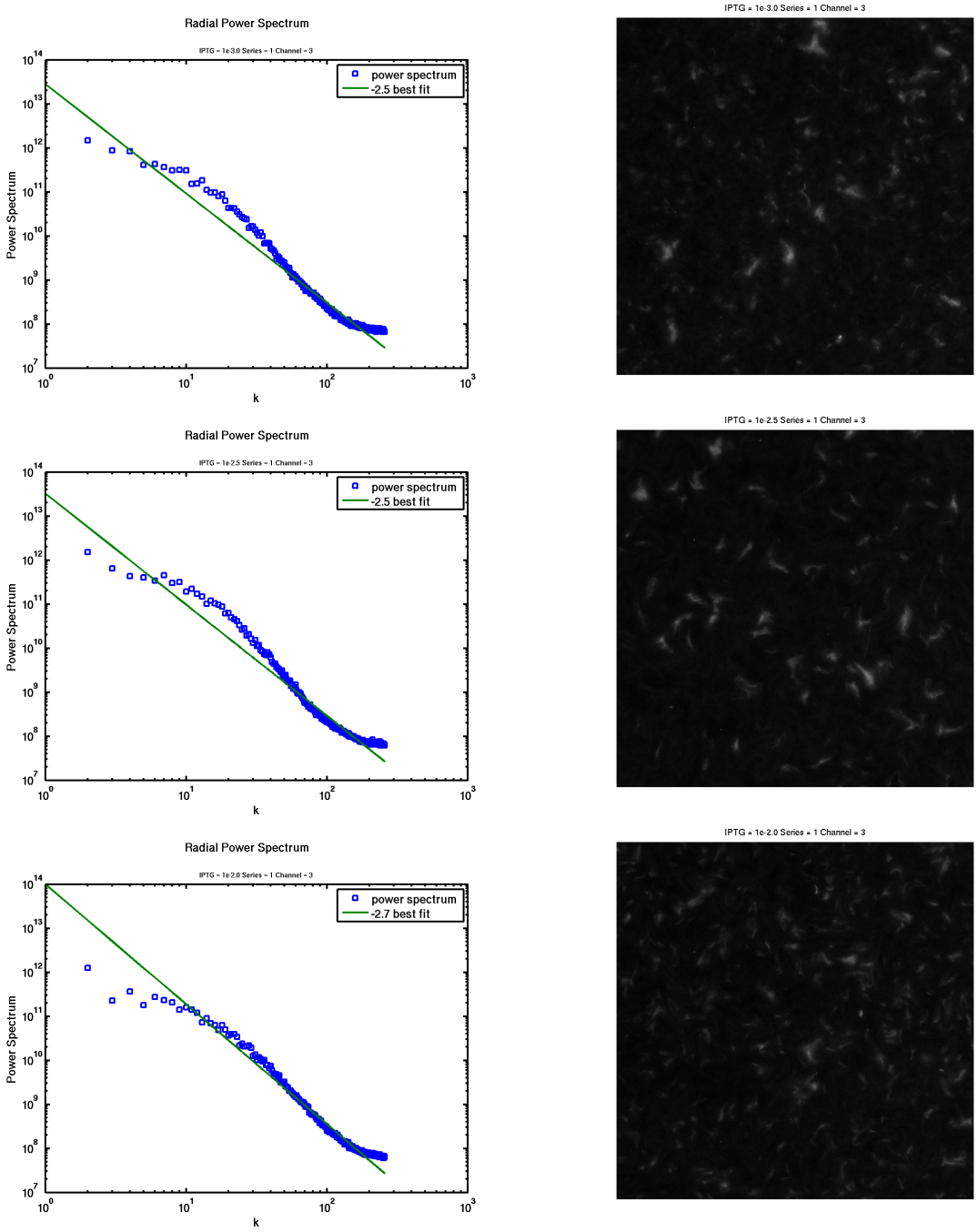

Fig. S14. RFP images and their corresponding Radial Power spectrums with powerlaw tail fits of -2.5, -2.5, -2.9 for IPTG concentrations of 10^{-3} M, $10^{-2.5}$ M, and 10^{-2} M respectively.

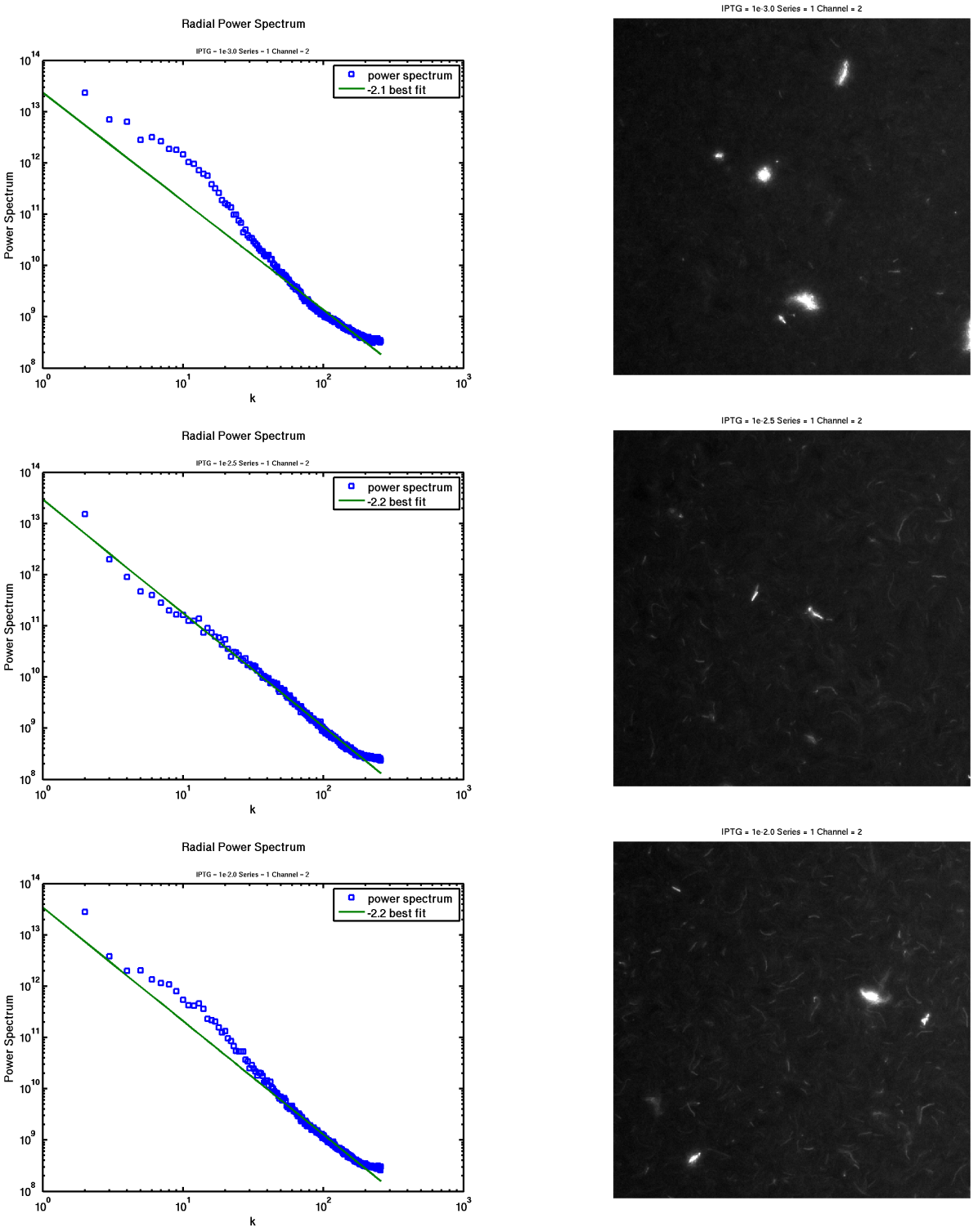

Fig. S15. GFP images and corresponding Radial Power spectrums with a powerlaw tail fits of -2.1, -2.2, -2.2 for IPTG concentrations of 10^{-3} M, $10^{-2.5}$ M, and 10^{-2} M respectively. At IPTG concentrations smaller than 10^{-4} M The green channel begins to look spatially homogeneous as the signal is not strong enough to show-up beyond the background camera noise.

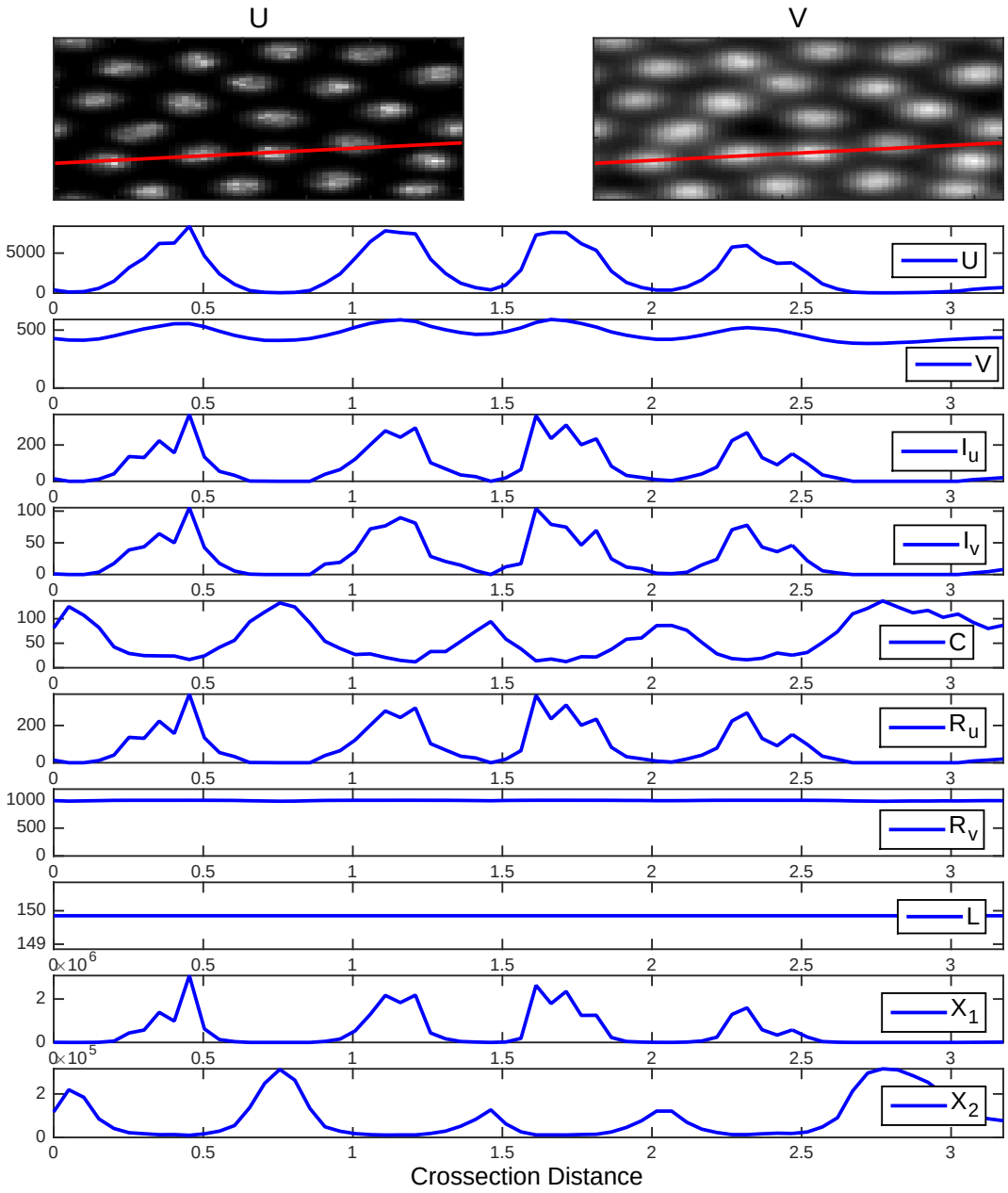

Fig. S16. $A_{3OC12HSL}$ and I_{C4HSL} patterns produced in our stochastic simulation using the parameters given in Tables S6-S7. The red line indicates the location of the cross-section used for all other dynamic variables. Cross-sectional slices of variables U ($A_{3OC12HSL}$), V (IC4HSL), I_u (LasI), I_v (RhlI), C (CI), R_u (LasR), R_v (RhlR), L (free LacI), X_1 (LasR-$A_{3OC12HSL}$ complex), and X_2 (RhlR-I_{C4HSL} complex).

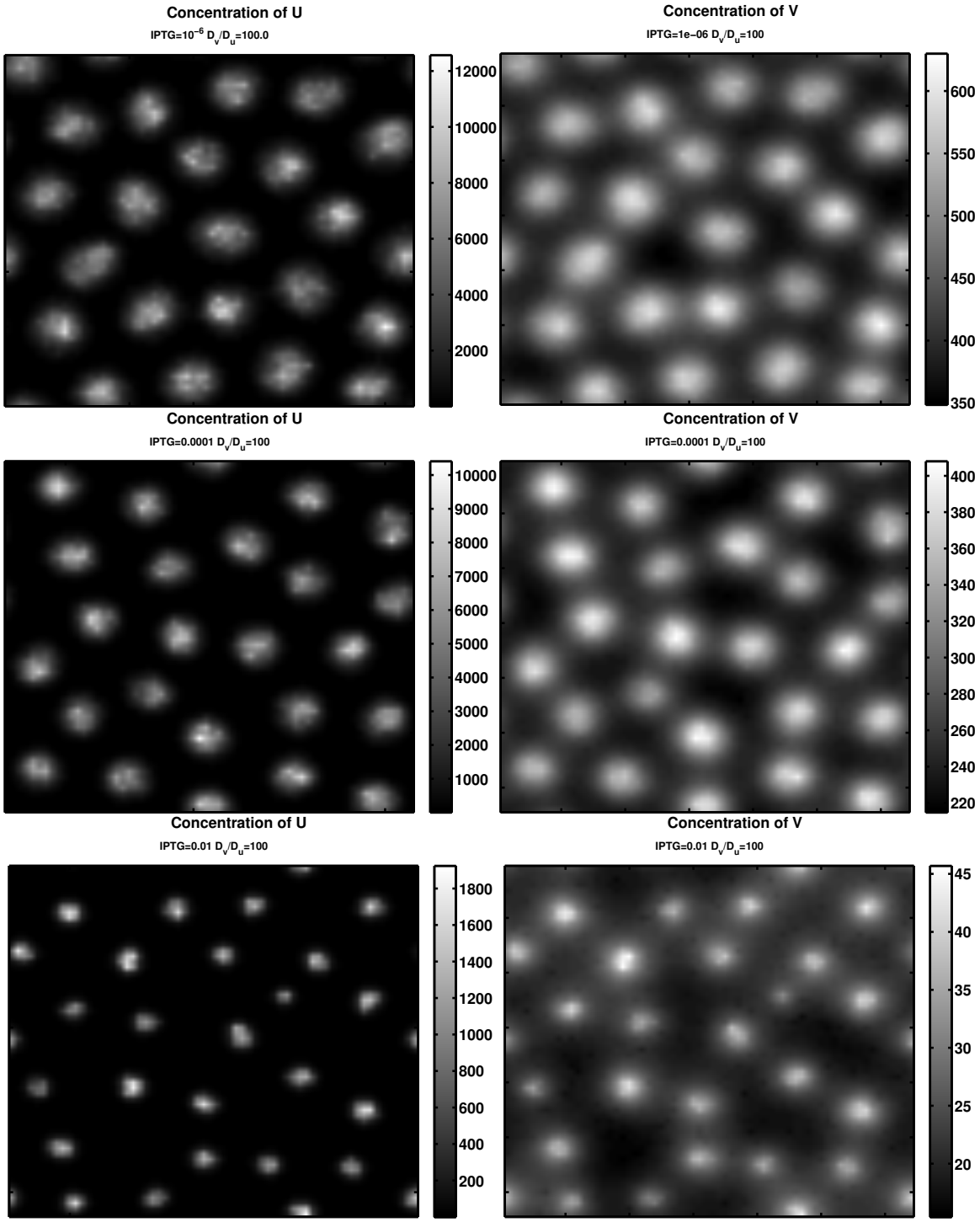

Fig. S17. $A_{3OC12HSL}$ patterns produced in our stochastic simulation using $D_v/D_u = 100$ and the parameters given in Tables S6-S7 for three different concentrations of IPTG.

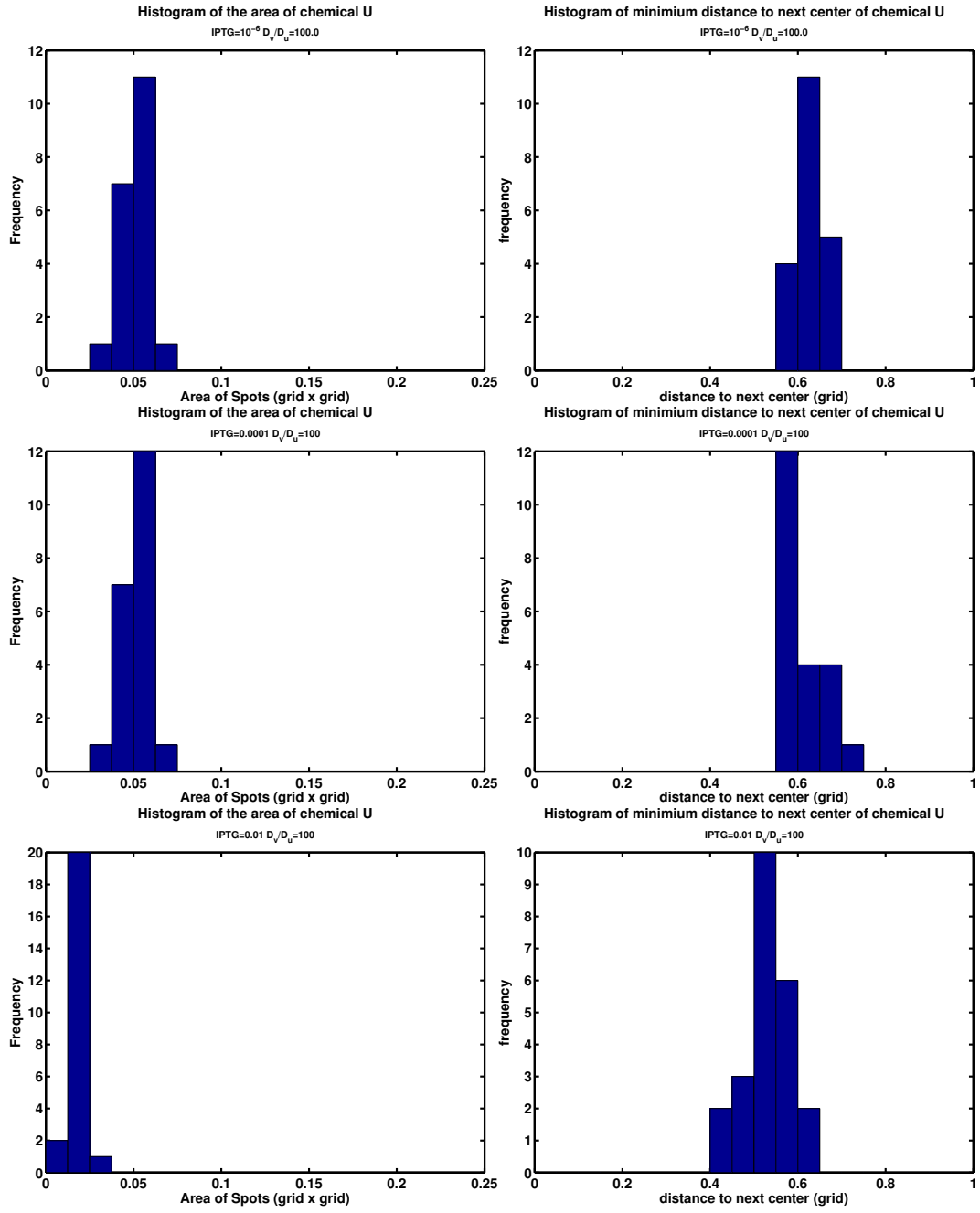

Fig. S18. Spot size and spacing distributions for 30C12HSL produced in our stochastic simulation with $D_v/D_u = 100$ for three different values of IPTG.

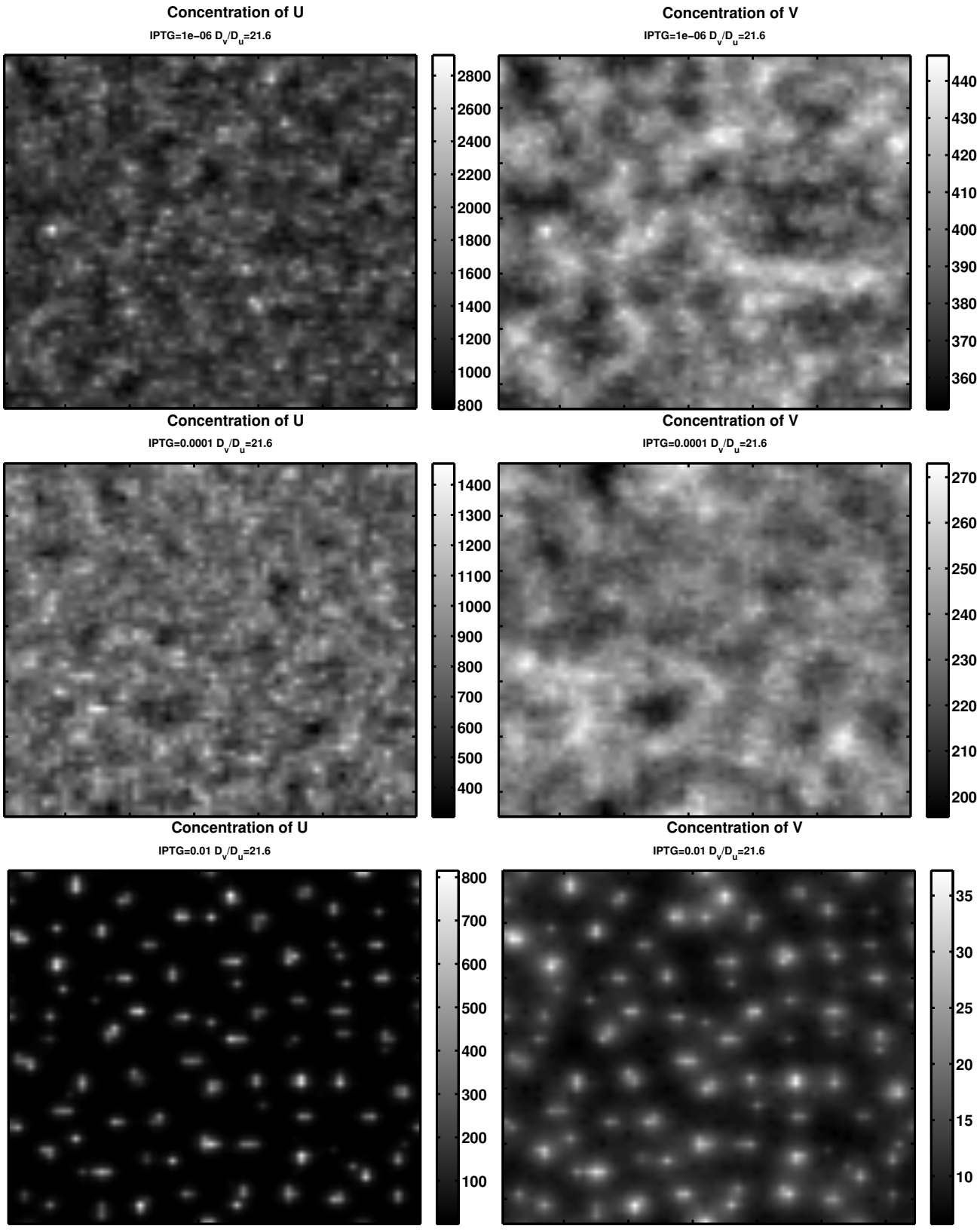

Fig. S19. $A_{3OC12HSL}$ patterns produced in our stochastic simulation using the measured diffusion ratio of $D_v/D_u = 21.6$ and the parameters given in Tables S6-S7 for three different concentrations of IPTG.

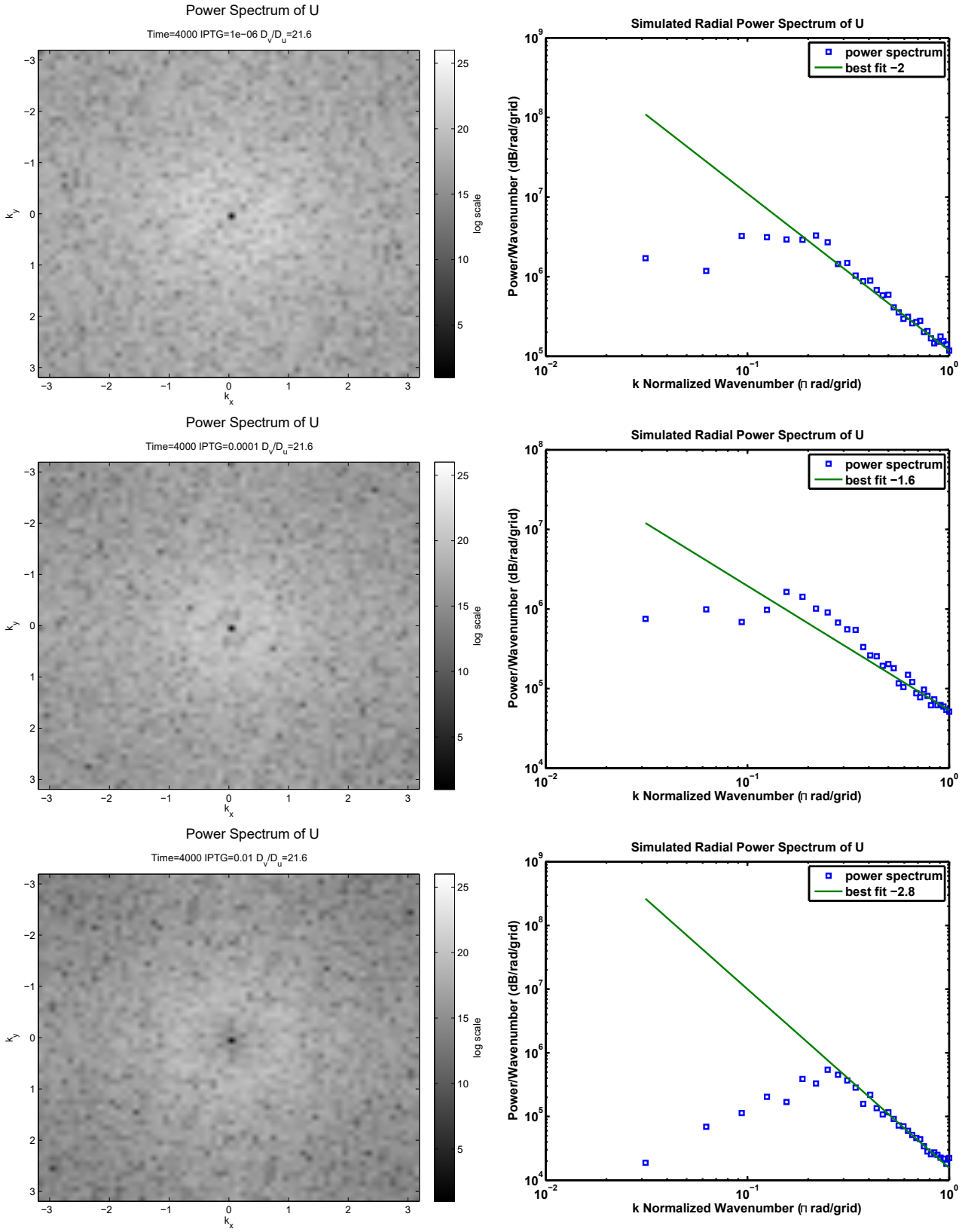

Fig. S20. 2D power spectrum and radial power spectrum for 30C12HSL produced in our stochastic simulation using $D_v/D_u = 21.6$ for three different values of IPTG.

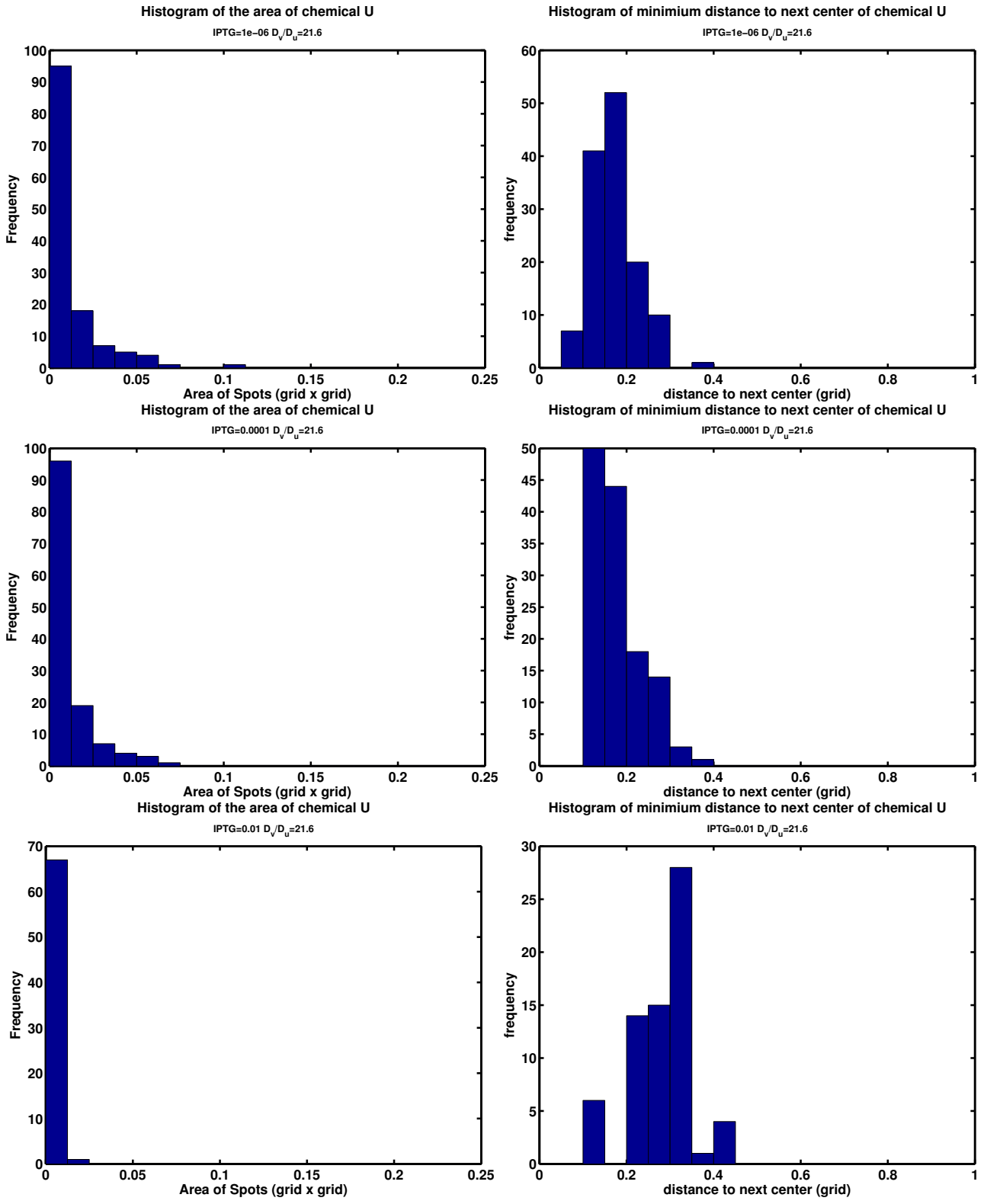

Fig. S21. Spot size and spacing distributions for 30C12HSL produced in our stochastic simulation using $D_v/D_u = 21.6$ for three different values of IPTG.

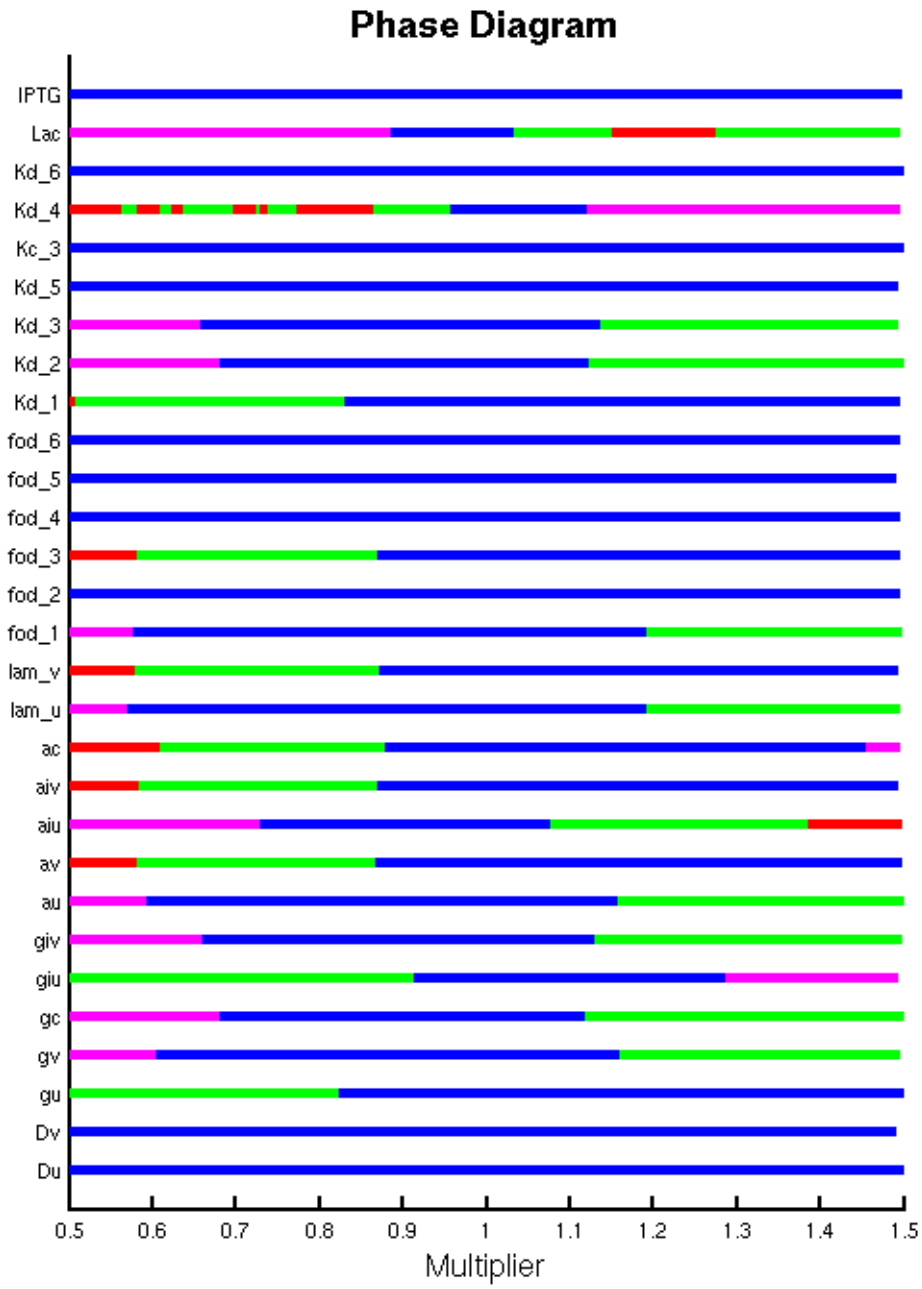

Fig. S22. Phase Diagram showing the type of phase as each parameter is varied from half of its nominal value to 1.5x its nominal value while keeping all other parameters fixed. Red indicates an unstable fixed point, magenta a stable homogeneous state, blue a stochastic pattern, and green deterministic Turing pattern.

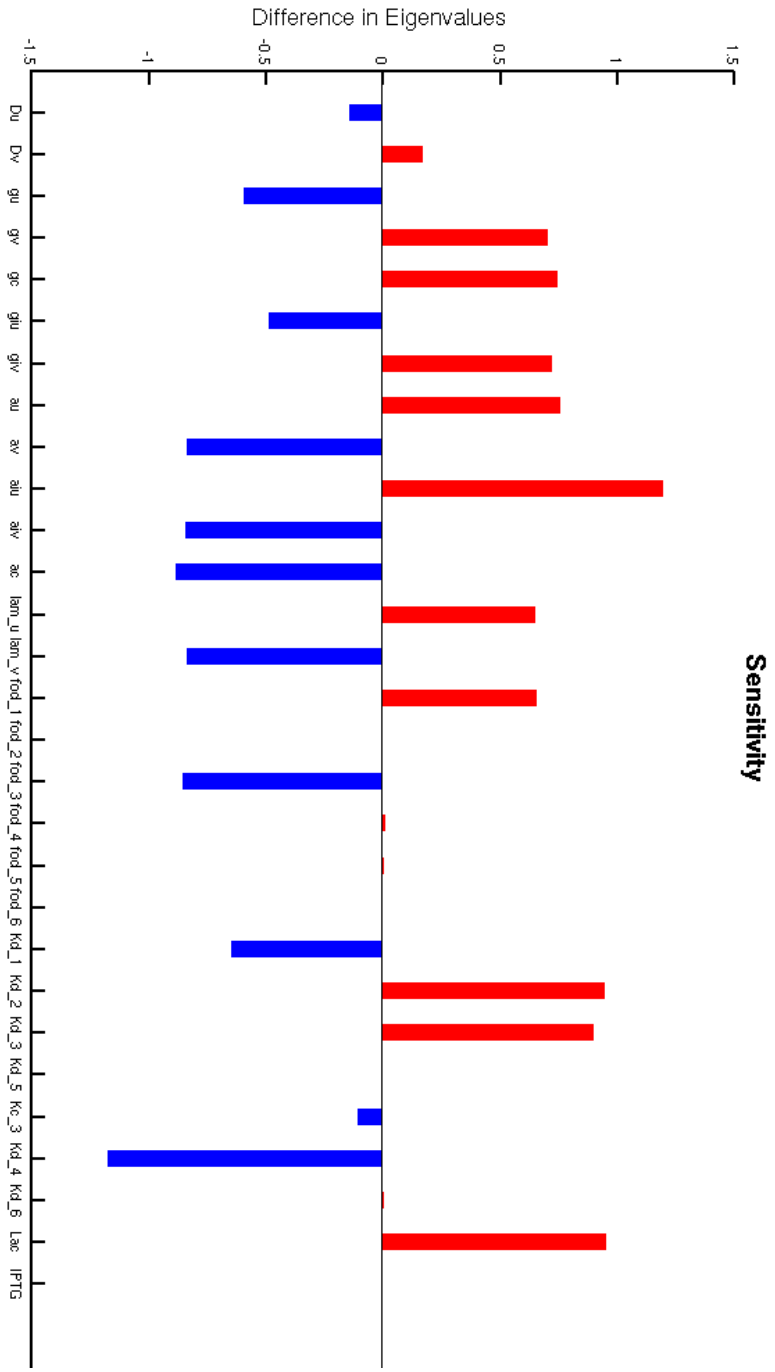

Fig. S23. Sensitivity of a phase to a parameter is indicated by plotting the difference in eigenvalues between 1.5x the nominal value of a parameter and half of the nominal value. Red indicates a parameter that when increased promotes traditional Turing patterns and blue indicates a parameter promoting stochastic patterns.

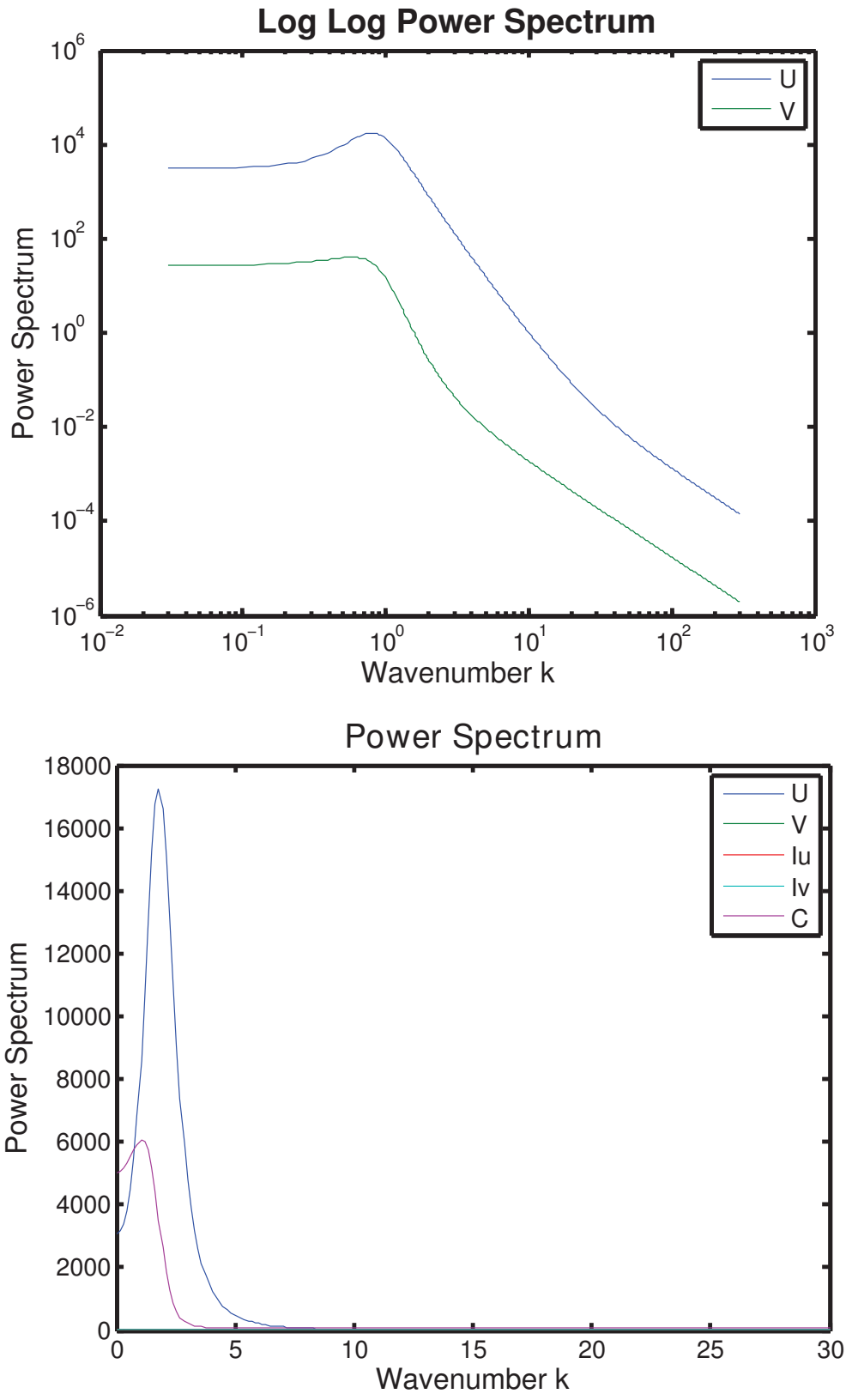

Fig. S24. The Analytic power spectrum calculated for the parameter set given in Tables S1-S2.

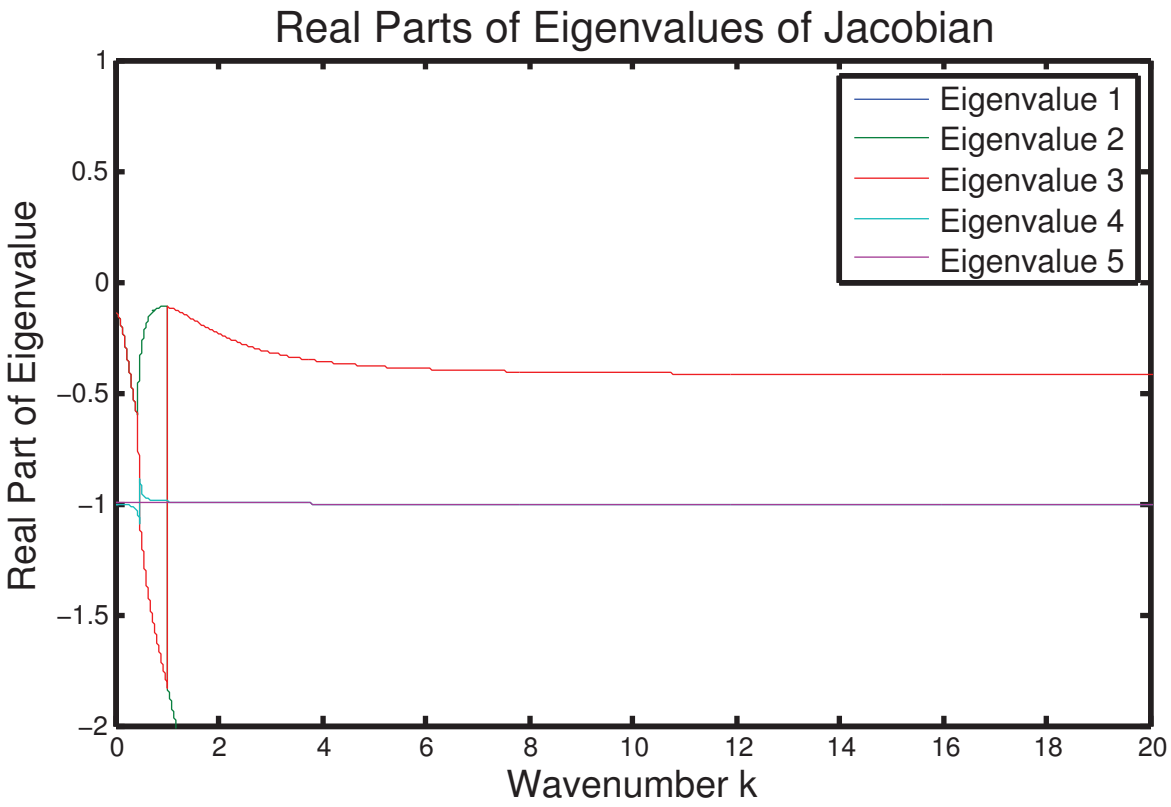

Fig. S25. The real part of the eigenvalues of the Jacobian for the parameter set given in Tables S1-S2 plotted as a funtion of k. All the eigenvalues are negative indicating that the pattern formed is stochastic.